Received: 21 November 2019 | Revised: 18 June 2020 | Accepted: 25 July 2020

DOI: 10.1002/hipo.23254

RESEARCH ARTICLE

WILEY

Recurrent amplification of grid-cell activity

Tiziano D'Albis[1] | Richard Kempter[1,2,3]

[1]Institute for Theoretical Biology, Department of Biology, Humboldt-Universität zu Berlin, Berlin, Germany

[2]Bernstein Center for Computational Neuroscience, Berlin, Germany

[3]Einstein Center for Neurosciences, Berlin, Germany

Correspondence
Tiziano D'Albis, Institute for Theoretical Biology, Department of Biology, Humboldt-Universitat zu Berlin, Berlin, Germany.
Email: tiziano.dalbis@gmail.com

Funding information
Bundesministerium für Bildung und Forschung, Grant/Award Number: 01GQ1705; Deutsche Forschungsgemeinschaft, Grant/Award Numbers: 327654276-SFB1315, KE788/3-1-SPP 1665

Abstract

High-level cognitive abilities such as navigation and spatial memory are thought to rely on the activity of grid cells in the medial entorhinal cortex (MEC), which encode the animal's position in space with periodic triangular patterns. Yet the neural mechanisms that underlie grid-cell activity are still unknown. Recent in vitro and in vivo experiments indicate that grid cells are embedded in highly structured recurrent networks. But how could recurrent connectivity become structured during development? And what is the functional role of these connections? With mathematical modeling and simulations, we show that recurrent circuits in the MEC could emerge under the supervision of weakly grid-tuned feedforward inputs. We demonstrate that a learned excitatory connectivity could amplify grid patterns when the feedforward sensory inputs are available and sustain attractor states when the sensory cues are lost. Finally, we propose a Fourier-based measure to quantify the spatial periodicity of grid patterns: the grid-tuning index.

KEYWORDS

amplification, entorhinal cortex, grid cells, grid-tuning index, Hebbian learning

1 | INTRODUCTION

Grid cells are neurons of the medial entorhinal cortex (MEC) that are tuned to the animal's position in the environment and whose firing fields form a periodic triangular pattern in space (Hafting, Fyhn, Molden, Moser, & Moser, 2005). Since their discovery, grid cells are believed to support high-level cognitive processes, such as navigation and spatial memory (e.g., Gil et al., 2018; Mathis, Herz, & Stemmler, 2012; McNaughton, Battaglia, Jensen, Moser, & Moser, 2006; Ólafsdóttir, Carpenter, & Barry, 2016; Tennant et al., 2018). Yet it remains unclear how grid-cell activity is formed and how it is processed within the entorhinal cortex (Rowland, Roudi, Moser, & Moser, 2016).

To gain mechanistic insights into the dynamics of grid-cell activity, recent experimental work has focused on the characterization of excitatory microcircuits in the superficial layers of the MEC (layers II and III), where grid cells are most abundant (Boccara et al., 2010). In particular, recurrent excitation has been described in layer II (Fuchs et al., 2016; Schmidt et al., 2017; Winterer et al., 2017), where it was previously thought to be very sparse or absent (Couey et al., 2013; Dhillon & Jones, 2000; Pastoll, Solanka, van Rossum, & Nolan, 2013). Anatomically, Schmidt et al. (2017) found that more than one third of the synaptic targets of a typical layer II principal cell are onto excitatory neurons of the same layer. Physiologically, Winterer et al. (2017) reported a 2.5% connectivity rate among layer II stellate cells and a 3% connectivity rate among layer III pyramidal cells.

Although anatomical and in vitro studies could not assess the spatial tuning of the connected neurons, two lines of evidence suggest that the observed recurrent excitatory connectivity is relevant for grid cells in vivo. First, grid-cell firing patterns are functionally coupled, that is, grids are organized in distinct functional modules with common scale and orientation (Hafting et al., 2005; Stensola et al., 2012), and co-modular grids react in concert to external manipulations of

the environment (Stensola et al., 2012; Yoon et al., 2013). Second, the spiking activity of grid cells with similar spatial phases is temporally correlated beyond simple firing-rate covariations (Dunn, Mørreaunet, & Roudi, 2015; Tocker, Barak, & Derdikman, 2015) and such correlations persist across network states (Gardner, Lu, Wernle, Moser, & Moser, 2019; Trettel, Trimper, Hwaun, Fiete, & Colgin, 2019). Grid-cell couplings could also arise via disynaptic inhibition (Couey et al., 2013), a hypothesis which is consistent with the facts that inhibition is predominantly local and that grid phases cluster in anatomical space (Gu et al., 2018; Heys, Rangarajan, & Dombeck, 2014). However, parvalbumin-positive (PV^+) interneurons, which provide strong perisomatic inhibition to entorhinal principal cells (Beed et al., 2013; Couey et al., 2013; Fuchs et al., 2016), including grid cells (Buetfering, Allen, & Monyer, 2014; Miao, Cao, Moser, & Moser, 2017), show neither grid-phase specific recurrent connectivity nor spatially periodic tuning (Buetfering et al., 2014). In summary, experimental evidence suggests that grid cells in the superficial layers of the MEC are strongly excitatorily connected and that these connections are grid-phase specific. But what could be the function of such recurrent connections?

Recurrent connectivity is at the core of continuous-attractor network (CAN) models for the origin of grid-cell patterns (e.g., Burak & Fiete, 2009; Couey et al., 2013; Fuhs & Touretzky, 2006; Guanella, Kiper, & Verschure, 2007; McNaughton et al., 2006; Navratilova, Giocomo, Fellous, Hasselmo, & McNaughton, 2012; Pastoll et al., 2013; Widloski & Fiete, 2014). CAN models assume that recurrent collaterals generate bumps of neural activity at the population level, and that such bumps are then translated across the network via self-motion inputs—thereby forming single-cell grids. The idea that self-motion inputs can sustain grid patterns is motivated by the facts that mammals can use path integration for navigation (Etienne & Jeffery, 2004), that speed and head-direction signals have been recorded within the MEC (Kropff, Carmichael, Moser, & Moser, 2015; Sargolini et al., 2006), and that grid-firing fields often persist in darkness (Barry, Ginzberg, O'Keefe, & Burgess, 2012; Hafting et al., 2005); but see also (Chen, Manson, Cacucci, & Wills, 2016; Pérez-Escobar, Kornienko, Latuske, Kohler, & Allen, 2016). Nevertheless, the attractor theory alone cannot explain how grids are anchored to the environment to avoid path-integration drifts (Burak & Fiete, 2009), and how grids align and distort in relation to the geometry of the enclosure (Barry, Hayman, Burgess, & Jeffery, 2007; Krupic, Bauza, Burton, & O'Keefe, 2016; Savelli, Yoganarasimha, & Knierim, 2008). Although CANs can be anchored to the physical space via spatially tuned inputs, for example, place or border cells (Guanella et al., 2007; Hardcastle, Ganguli, & Giocomo, 2015; Ocko, Hardcastle, Giocomo, & Ganguli, 2018; Pastoll et al., 2013; Welinder, Burak, & Fiete, 2008), all these models fall short in explaining how a path-integrating network may develop in the first place.

Alternatively, grid-cell activity could arise in a feedforward network prior to the development of the recurrent connections (e.g., Castro & Aguiar, 2014; D'Albis & Kempter, 2017; Dordek, Soudry, Meir, & Derdikman, 2016; Mhatre, Gorchetchnikov, & Grossberg, 2012; Monsalve-Mercado & Leibold, 2017; Stepanyuk, 2015; Weber & Sprekeler, 2018). In this case, single-cell grids may spontaneously emerge via three simple ingredients: (a) spatially tuned feedforward inputs; (b) Hebbian synaptic plasticity; and (c) a cell-intrinsic mechanism that generates spatial periodicity, for example, firing-rate adaptation (D'Albis & Kempter, 2017; Kropff & Treves, 2008), phase precession (Monsalve-Mercado & Leibold, 2017), or excitation/inhibition balance (Weber & Sprekeler, 2018). A strength of these models is that they can explain how a grid-cell circuit develops in a self-organized manner. Additionally, because the feedforward inputs are sensory driven, the resulting grid patterns are naturally anchored to physical space and follow geometrical deformations of the spatial enclosure.

In this article, we assume that noisy grid patterns initially emerge in a feedforward circuit. We hypothesize that, after such rudimentary grids are formed, neurons with similar tuning properties (i.e., grid scale, orientation, and phase) develop recurrent excitatory connections that improve the spatial regularity of the feedforward grids. Such an amplification mechanism may be required to improve the periodicity of irregular multi-peak firing patterns during development (Langston et al., 2010; Wills, Cacucci, Burgess, & O'Keefe, 2010) and/or to sharpen noisy grid signals that emerged upstream of the MEC, such as in pre- and parasubiculum (Boccara et al., 2010). In other words, we propose that recurrent excitation in the MEC could amplify grid-cell activity, alike feedback connectivity in V1 was shown to amplify orientation tuning formed by thalamic afferents (e.g., Ben-Yishai, Bar-Or, & Sompolinsky, 1995; Carandini & Ringach, 1997; Douglas, Koch, Mahowald, Martin, & Suarez, 1995; Ko et al., 2013; Lien & Scanziani, 2013; Murphy & Miller, 2009; Somers, Nelson, & Sur, 1995; Suarez, Koch, & Douglas, 1995). We further hypothesize that such a learned recurrent connectivity could support attractor dynamics when the feedforward tuning is lost, thereby providing a basis for the development of a path-integrating system.

We test these hypotheses in a computational model. First, we simulate the emergence of a recurrent connectivity structure in a biologically realistic network of noisy grid cells. We show that the learned recurrent connections could amplify feedforward grids (Section 2.1) and maintain attractor states in the absence of feedforward tuning (Section 2.2). To quantify gridness, we introduce a new Fourier-based measure—the grid-tuning index—and show that it is more convenient than the classical gridness score (Langston et al., 2010). Next, we study how the learning and amplification dynamics depend on the properties of the feedforward inputs (Sections 2.3 and 2.4). Finally, we present a reduced one-dimensional (1D) model for the recurrent amplification of grid-cell activity on linear tracks (Appendix A). This reduced model explains the main features of grid-pattern amplification, is analytically tractable, and can be understood intuitively.

2 | RESULTS

To study the amplification of grid-cell activity in the MEC, we model a firing-rate network comprising a population of $N_E = 900$ excitatory neurons (E) and a population of $N_I = 225$ inhibitory neurons (I). The modeled network roughly matches the size of a local microcircuit within a grid-cell module in MEC layer II, for example, a cluster of calbindin-positive pyramidal cells or a population of reelin-positive stellate cells between those clusters (Fujimaru & Kosaka, 1996; Gu

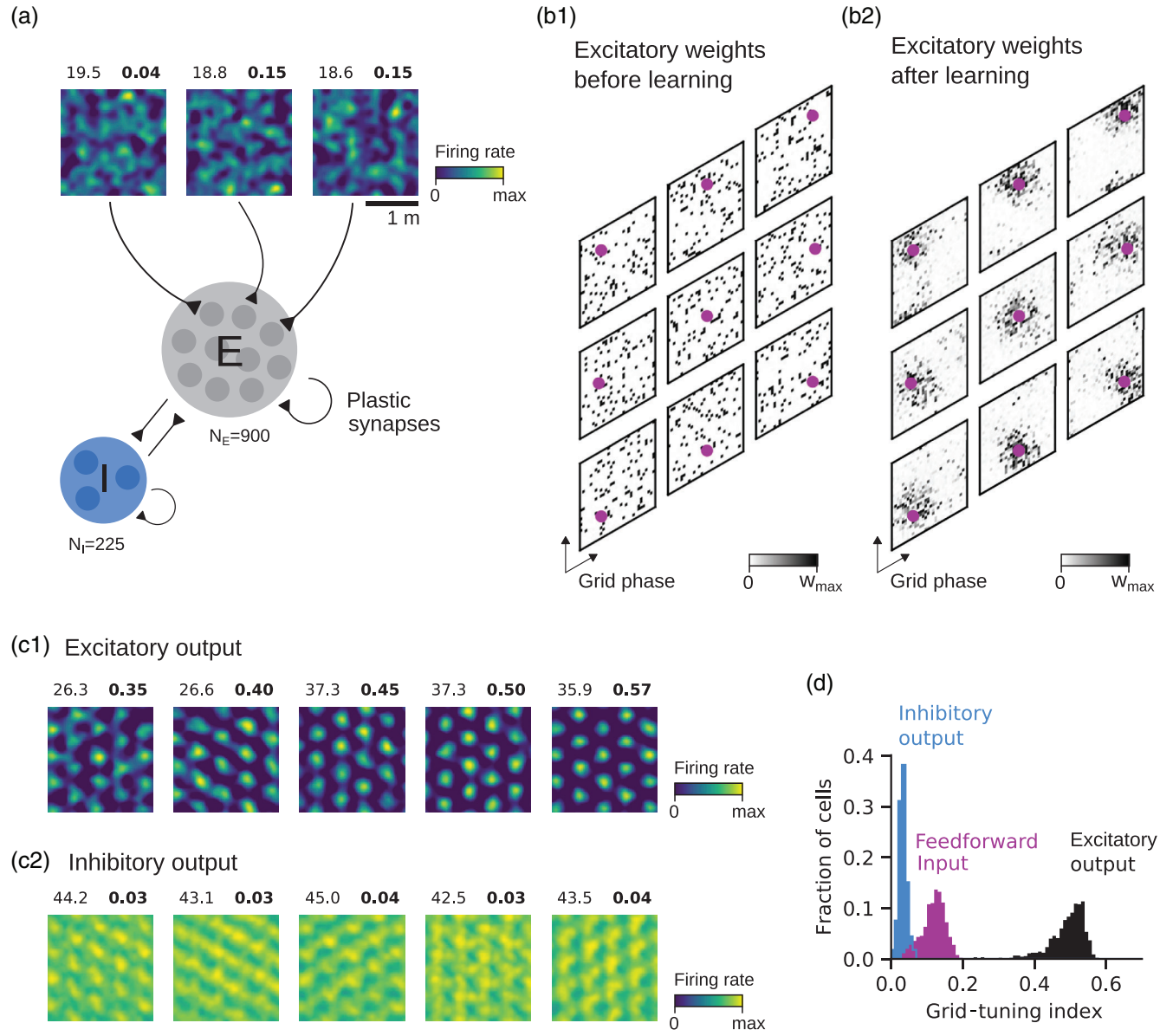

FIGURE 1 Model of recurrent amplification of grid-cell activity. (a) Model schematic. We model the activity of a population of N_E = 900 excitatory neurons (E, dark-gray disks) and a population of N_I = 225 inhibitory neurons (I, dark-blue disks). The total feedforward input to each excitatory neuron is a noisy grid as a function of space (three example firing-rate maps at the top, max firing-rates in spikes/s at the top-left corner, grid-tuning indexes at the top-right corner). The synaptic connectivity is sparse and initially random (10% connectivity in the $E \to E$ pathway, and 40% connectivity in the $E \leftrightarrow I$ and $I \to I$ pathways). The recurrent excitatory weights undergo Hebbian plasticity, whereas all other synapses are held fixed. (b) Recurrent excitatory connectivity before learning (b1) and after learning (b2). The excitatory connections to nine example principal cells are shown (small rhombi). Nearby pixels in a synaptic-weight map correspond to cells with similar grid phases. The magenta dot marks the phase of the total feedforward input. (c) Firing-rate maps of five example excitatory (c1) and inhibitory (c2) neurons at the steady-state of the recurrent dynamics. Maximal firing rates (in spikes/s) at the top-left corner, grid-tuning indexes at the top-right corner. (d) Distributions of the grid-tuning index for the feedforward inputs (magenta), the steady-state inhibitory outputs (light blue), and the steady-state excitatory outputs (black). See Section 4 for further details and Table 1 for parameter values [Color figure can be viewed at wileyonlinelibrary.com]

et al., 2018; Kitamura et al., 2014; Naumann et al., 2016; Ray et al., 2014). Excitatory and inhibitory neurons are mutually coupled and recurrently connected locally (Figure 1a, see Section 4.1 for details). The synaptic connectivity is sparse and initially random. Additionally, the recurrent excitatory connections are plastic.

We assume that the excitatory cells receive spatially tuned feedforward inputs. The total feedforward input to each excitatory cell is a noisy grid as a function of space (three example firing-rate maps in Figure 1a; see Section 4.2 for details). Such noisy grid patterns could spontaneously emerge in an upstream feed forward network (not shown in Figure 1a) via spatially tuned sensory inputs, Hebbian synaptic plasticity, and experience (see e.g., D'Albis & Kempter, 2017; Kropff & Treves, 2008; Weber & Sprekeler, 2018). To abstract from the specific mechanism that generates this tuning, we

model feedforward inputs as periodic grids distorted by a blanket of spatial noise. The noise models spatial irregularities that could arise from uneven sensory coverage during learning or from non-grid spatial inputs (Diehl, Hon, Leutgeb, & Leutgeb, 2017). We assume that noisy grids have distributed spatial phases but share similar spacing and orientation, alike to grid-cells within a module (Hafting et al., 2005; Stensola et al., 2012). Note that grid-cell modularity is assumed to have already emerged upstream (Urdapilleta, Si, & Treves, 2017). Each excitatory neuron in the network is labeled by the spatial phase of its feedforward input, which we call the *preferred phase* of a neuron. With respect to these preferred phases, the recurrent excitatory connections are initially random (Figure 1b1).

2.1 | Recurrent amplification of grid-cell activity

We hypothesize that correlations in the feedforward inputs may generate a structured recurrent connectivity among the excitatory cells, and that this connectivity could amplify grid patterns. To test this hypothesis, we simulate the development of the recurrent excitatory weights under a Hebbian learning rule while a virtual rat performs a random walk in the environment. The plasticity rule strengthens synapses between neurons that are co-active, but keeps the total synaptic strength constant and the individual synaptic weights bounded (see Section 4.3 for details). Figure 1b illustrates such a learning process. Before learning, the recurrent excitatory connectivity is random (Figure 1b1), and there is no relation between the preferred phase of an excitatory cell (magenta dot) and the phases of its excitatory inputs (black pixels). After learning, however, a structure has emerged in the synaptic weights such that cells with similar preferred phases are strongly excitatorily connected (Figure 1b2).

Next, we test whether such a connectivity could amplify grid patterns. For simplicity, we first assume that the network's activity remains close to its steady state while the virtual rat explores the enclosure. This is because neural integration is typically much faster than systematic changes in the input activity for typical animals' exploration speeds, and because the input tuning is assumed to be smooth in space. With these assumptions, we compute the steady-state activity of the network in all locations of the environment (10 example firing-rate maps in Figure 1c). We find that the excitatory neurons display a sharp grid tuning at the steady-state output (Figure 1c1), which was not present at the feedforward input (Figure 1a); see also Figure A3 in Appendix A for a similar effect in the reduced one-dimensional model. By contrast the inhibitory neurons fire at high rates throughout the environment and their grid tuning is weak (Figure 1c2).

To quantify the strength of grid tuning, we introduce the *grid-tuning index*. The grid-tuning index measures the strength of 60° periodicity of a spatial map from the pattern's spectral amplitude at its tuning harmonic normalized by the total firing rate in the environment (see Section 4.5 for details). The index approaches 1 for regular grids with infinitely small fields, and approaches 0 for completely aperiodic patterns. As compared to the commonly adopted gridness score (e.g., Hafting et al., 2005; Langston et al., 2010) the grid-tuning index has several advantages: (a) it is naturally bounded between 0 and 1; (b) it is modulated by the dynamic range of the activity; and (c) it can be computed analytically (see Section 4.5, for a systematic comparison between the new grid-tuning index and the classical gridness score).

Figure 1d shows the distribution of the grid-tuning index for all input and output patterns. We note that the excitatory outputs (black) show larger grid-tuning indexes compared to both feedforward inputs (magenta) and inhibitory outputs (light blue). Although a periodic pattern is visible in the inhibitory maps (Figure 1c2), such tuning is very weak compared to the overall firing rate in the environment and leads to low grid-tuning indexes (Figure 1d, light blue). This result is consistent with the experimental observation that parvalbumin-positive inhibitory neurons in the MEC are not grid tuned (Buetfering et al., 2014).

To evaluate whether recurrent dynamics is fast enough to improve grid tuning in more natural settings, we simulate the network's activity for a virtual rat that continuously moves in the environment. For clarity, we first simulate a straight virtual-rat trajectory at constant speed across the enclosure (dashed arrows in Figure 2a). Figure 2b1 shows the results of this simulation for one example excitatory cell. We can see that the output firing rate of the cell (green) is the result of a weakly grid-tuned feedforward input (magenta), a strongly grid-tuned recurrent excitation (gray), and a flat recurrent inhibition (light blue). As a result, the grid tuning is considerably amplified at the output. We also find that such an amplification persists when the network's activity is modulated by the so-called *theta rhythm* (Figure 2b2)—an oscillation at 4–12 Hz that strongly paces grid-cell activity in the MEC (Boccara et al., 2010; Hafting, Fyhn, Bonnevie, Moser, & Moser, 2008). The robustness of this result is tested by simulating the theta-modulated network's dynamics for a random walk of the virtual rat across the entire enclosure (see Section 4.4 for details on the spatial exploration model). In this scenario, we find that the excitatory cells have grid-tuning indexes that are slightly smaller than the ones obtained at the steady-state output, but considerably larger than the ones at the feedforward input (Figure 2c).

We conclude that a recurrent network with plastic excitatory synapses can spontaneously self-organize to amplify grid-cell activity and that this amplification can occur within a single cycle of the theta rhythm.

2.2 | Attractor dynamics in the absence of input tuning

To outline the relationship between our model and CAN models of grid-cell activity, we now test whether the recurrent excitatory connections that emerged via Hebbian learning also support attractor dynamics when the feedforward tuning is turned OFF. To this end, we simulate the network with fixed synaptic connectivity and in the absence theta modulation for a straight virtual-rat trajectory. Figure 3a shows the network's population feedforward input (top row) and population output (bottom row) at different time points in the simulation.

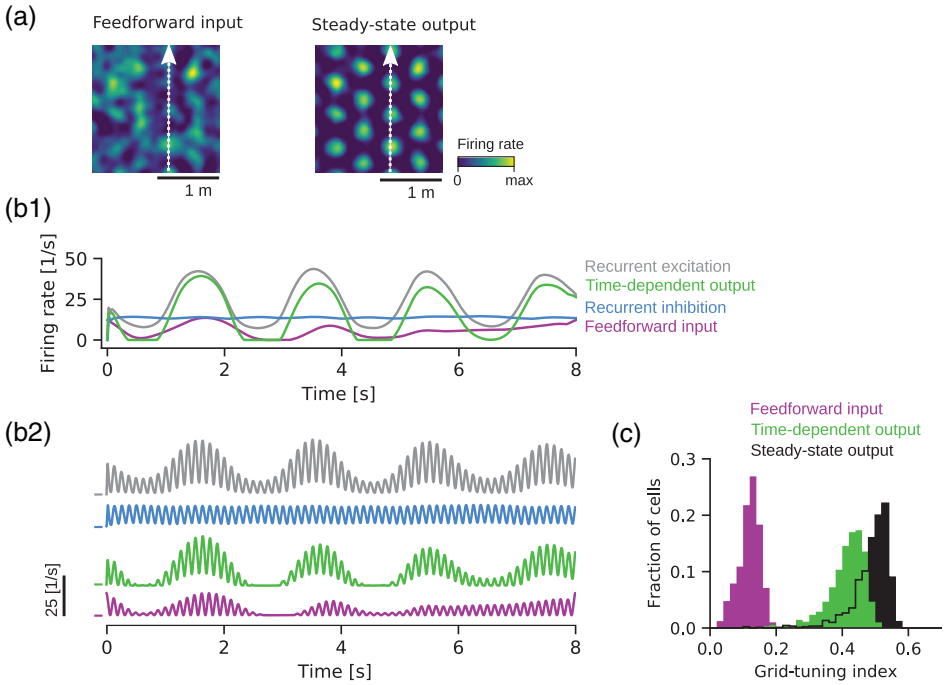

FIGURE 2 Temporal dynamics of grid-pattern amplification. (a) Example of a straight virtual-rat trajectory (dashed arrow) superimposed on the total feedforward input (left) and steady-state output (right) of one excitatory cell. (b) Time-dependent activity of the excitatory cell in panel (a) as the virtual rat moves in the arena. The activity is shown both without (b1) and with (b2) theta modulation. Magenta: feedforward input; gray: total recurrent excitatory input; light blue: total recurrent inhibitory input; green: time-dependent output. The total (excitatory and inhibitory) recurrent inputs are the weighted sums of the firing rates of the upstream cells. Note that because the total synaptic weight of the $E \rightarrow I$ pathway is 0.4 (Table 1), the total inhibitory input is lower than the firing rate of a single inhibitory cell (Figure 1c2). The plots in panels (b1) and (b2) are on the same scale. The colored ticks in (b2) indicate the zero baseline for the respective curves. We assume a network integration time constant τ = 10 ms and a theta-modulation frequency f_θ = 8 Hz. (c) Distribution of the grid-tuning indexes of all excitatory neurons (green) for a walk of the virtual rat across the entire environment and theta-modulated activity. The grid-tuning indexes of the feedforward input (magenta) and steady-state output (black) are also shown for comparison; see also Figure 1d. See Section 4 for further details and Table 1 for parameter values [Color figure can be viewed at wileyonlinelibrary.com]

Initially (t < 4.1 s), the feedforward input is weakly grid tuned and, as a result, a noisy bump of activity is visible at the population input (Figure 3a, top row). This noisy bump moves across the network as the virtual rat moves in the arena and is amplified by the recurrent connections at the population output (Figure 3a bottom row and Figure 3b, for t < 4.1 s).

At time t = 4.1 s, we set the feedforward input to all the neurons at the same constant value (5 spikes/s), thereby simulating a temporary loss of the sensory input tuning. Crucially, after this switch, the output activity of the network maintains a localized bump of activity for the entire time interval in which the inputs remain untuned. This behavior is a defining feature of attractor networks. However, in the absence of input tuning, the output bump does not stay at the same location, but slowly drifts across the network and stabilizes at a location that depends on the particular recurrent connectivity that has been learned (Figure 3a,b1, from t = 4.1 s to t = 10.9 s). Finally, as soon as the input tuning is restored (Figure 3 for t > 10.9 s), the output bump rapidly moves towards the location dictated by the feedforward inputs.

In the absence of input tuning, the output bump drifts on a time scale of seconds, and the drift speed is highest within the first second after cue removal (Figure 3b1,b2, top). Yet the network maintains a memory of the bump location within a time scale of hundreds of milliseconds, which is much longer than the time scale of amplification (tens of milliseconds). Also note that the bump's peak rate settles to a level that is lower compared to the one in the tuned condition (Figure 3b2, bottom) and that (for the current choice of parameter values) the bump vanishes if the feedforward input is set to zero in the untuned condition.

The fact that the output bump drifts away from its original location when the input tuning is removed (although the network's dynamics is fully deterministic) suggests that network may have only a small set of attractors states. To assess the shape of the network's attractor landscape, we thus cued all possible locations in phase space by presenting an artificial feedforward bump to the network for 1 s. We then removed the cue and recorded the location of the output bump after 15 s, when the bump had settled. In Figure 3c, we show the locations where the bump has settled (black dots, attractors) and the normalized distance traveled by the bump (color coded). We find that there are typically three to four discrete attractor states in each network, and that their locations depend on the specific realization of the recurrent connectivity matrix. Consistently, the bump locations reached in the simulations of Figure 3a,b with untuned inputs are predicted by the numerically approximated attractor landscapes and

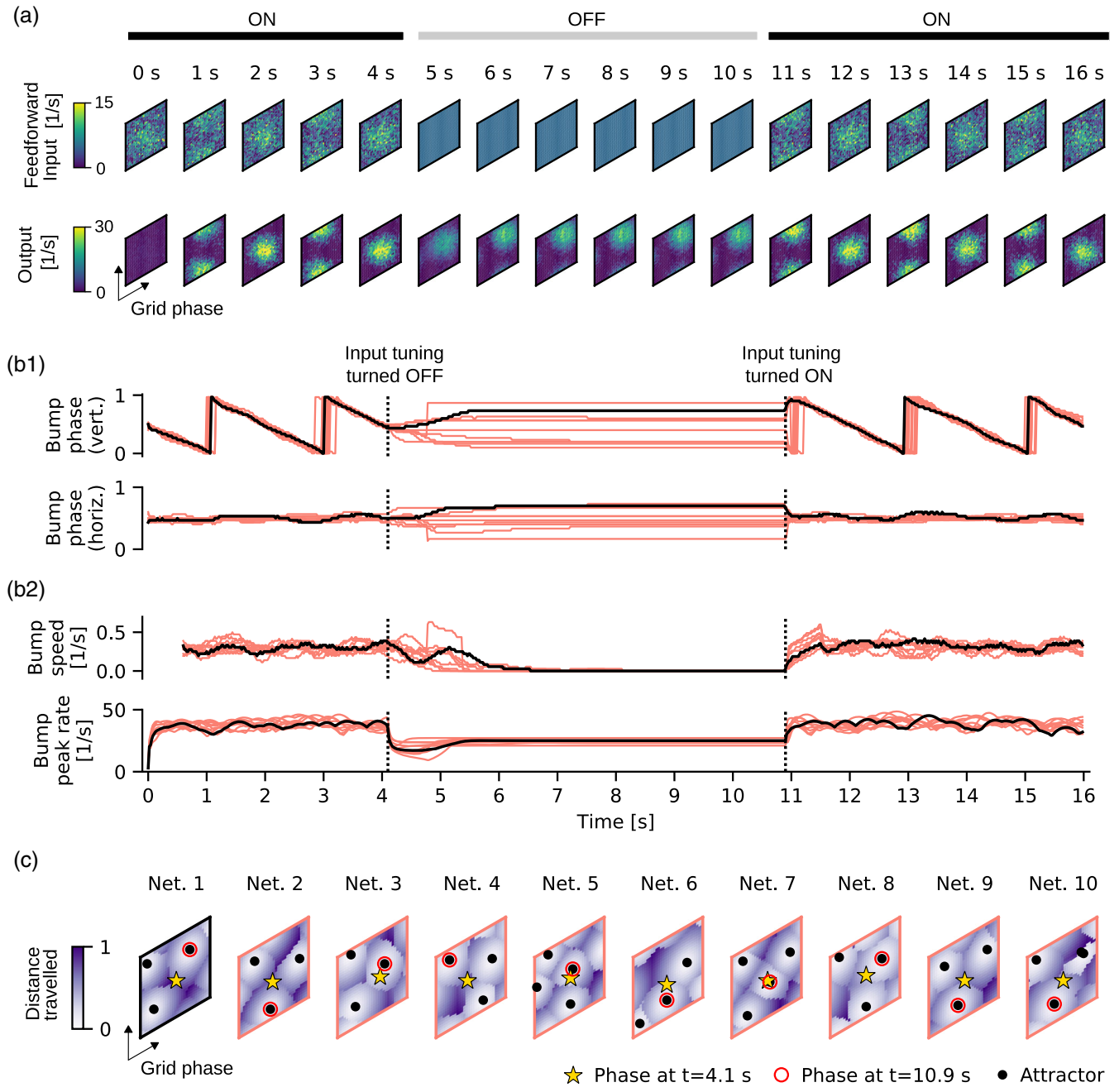

FIGURE 3 Attractor dynamics in the absence of input tuning. (a) Population feedforward input (top row) and population excitatory output (bottom row) at multiple time points in the simulation (time at the top) as a virtual rat walks at constant speed on a straight path (see also Figure 2a). Each rhomboidal firing-rate map shows the activity of all excitatory neurons in the network sorted by their preferred grid phase. For convenience, we assume here an arena with periodic boundaries. In the time intervals [0, 4.1] s and [10.9, 16] s, the feedforward inputs are noisy grids (input tuning ON, black bars on top). In the time interval [4.1, 10.9] s the feedforward inputs are set to a constant rate of 5 spikes/s (input tuning OFF, gray bar on top). The recurrent excitatory weights have been learned via Hebbian plasticity (Figure 1b2). (b1) Black: location of the population-output activity bump along the vertical (Vert., top) and horizontal (Horiz., bottom) coordinate of the phase space for the simulation in (a). The pink lines indicate the bump locations for networks whose recurrent weights were learned with different input-noise realizations. The dotted vertical lines indicate the times at which the feedforward tuning is switched OFF and ON. (b2) Black: speed (top) and peak firing rate (bottom) of the population-output activity bump for the simulation in (a). The pink lines denote the same quantities for recurrent connectivities learned with different input-noise realizations. The speed was smoothed with a rectangular window of length 600 ms; to exclude boundary effects due to filtering, the first 600 ms are not shown. (c) Attractor landscapes of 10 networks (Net. 1–10) with recurrent connectivities learned with different input-noise realizations. The left-most panel (Net. 1, black border) refers to the network shown in (a) and (b) (black lines). The remaining nine panels (Net. 2–10, pink borders) refer to the networks shown in (b) (pink lines). Each grid phase is color-coded according to the normalized distance traveled in the absence of input tuning by a bump cued at that phase. The cue was provided for 1 s and the distance traveled was measured 15 s after cue removal. The black dots denote the attractors of the network, that is, the bump locations reached 15 s after cue removal. The yellow star and the red circle denote the bump locations right before the input tuning is turned OFF (t = 4.1 s) and turned ON again (t = 10.9 s) for the simulations in panels (a) and (b). See Section 4 for further details and Table 1 for parameter values [Color figure can be viewed at wileyonlinelibrary.com]

by the bump phase at time t = 4.1 s (Figure 3c, yellow stars and red circles). These results suggest that our network supports attractor dynamics but does not allow for a continuum of attractor states as proposed in CAN models of grid-cell activity (e.g., Burak & Fiete, 2009; McNaughton et al., 2006).

In summary, we have shown that a network of noisy grid cells can develop structured recurrent connections that amplify grids when the feedforward tuning is present and support attractor dynamics otherwise. However, memories about bump locations decay after cue removal, because the network's attractor landscape is not flat.

2.3 | Effects of input tuning on amplification and learning

We now study how grid-pattern amplification and learning are affected by the tuning of the feedforward input. To this end, we vary the input-tuning strength β, which controls the regularity of the feedforward grids. For β = 0, input spatial patterns are completely noisy; for β = 1 they are regular triangular grids (five examples in Figure 4a1, see Section 4.2, for details). In experiments, the input-tuning strength could be modulated by the novelty of the environment or the availability of external sensory cues (e.g., visual landmarks).

In a first set of simulations, we assess the generalization capabilities of the network for different values of the input-tuning strength β and a fixed recurrent connectivity. This fixed connectivity has been learned with a reference value of β = 0.35 (Figure 1b2). Five example steady-state outputs are shown in Figure 4a2. We observe that output patterns are more spatially regular compared to the feedforward inputs, and that output grid-tuning indexes are larger than the inputs for all values of β (Figure 4b). We then estimate the improvement in grid-spatial tuning by computing the *grid-amplification index*, that is, the ratio between output and input grid-tuning indexes (Figure 4c). We observe up to a sixfold amplification for input-tuning strengths

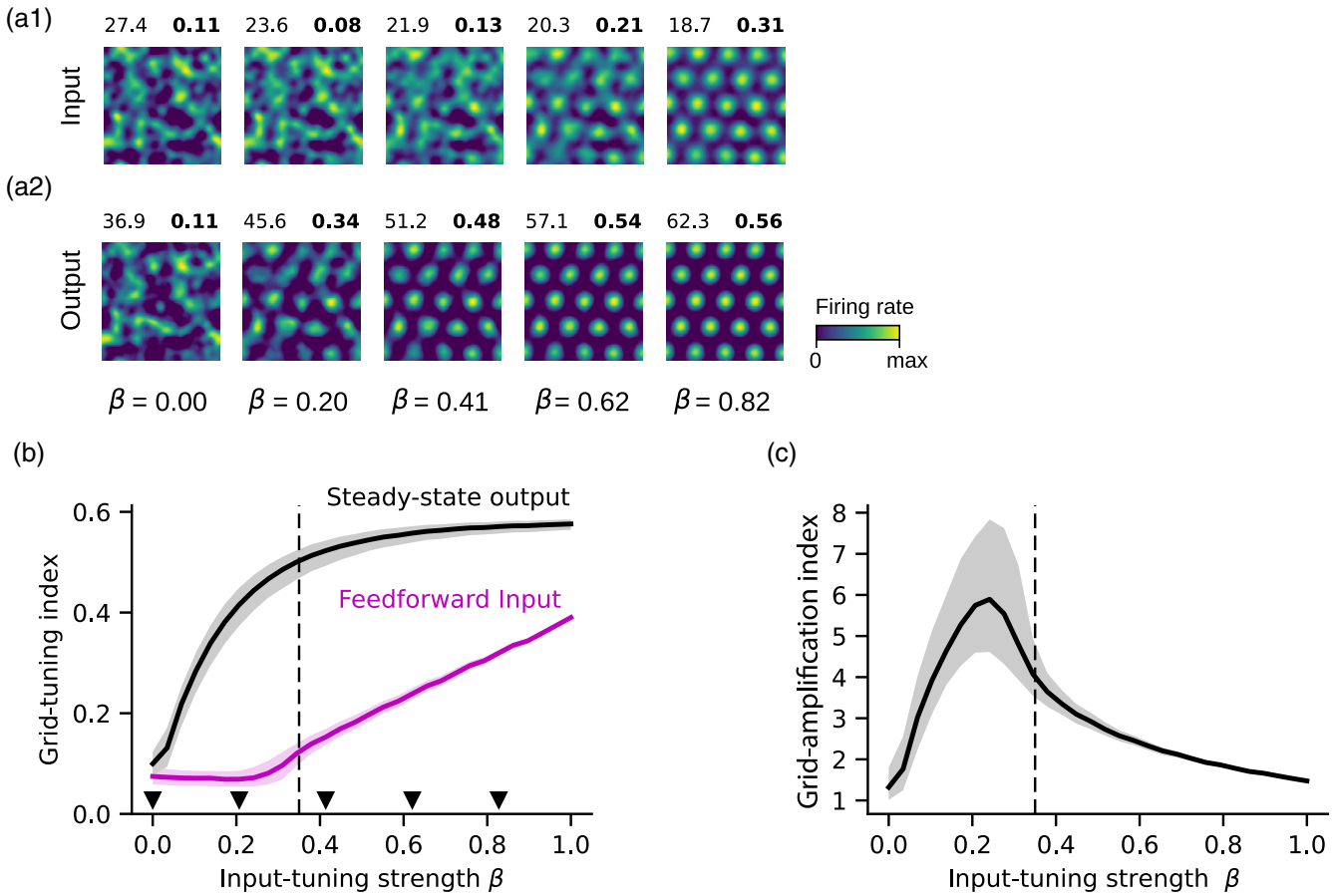

FIGURE 4 Effects of input tuning on grid-pattern amplification. (a) Example feedforward inputs (a1) and steady-state outputs (a2) for five values of the input-tuning strength β (see also triangles in (b)). Maximal firing rates in spikes/s at the top-left corner, grid-tuning indexes at the top-right corner. Output grid-tuning indexes are computed at the steady-state of the recurrent dynamics with fixed recurrent connectivity (Figure 1b2). The recurrent connectivity was learned with a reference value of the input-tuning strength β = 0.35 (vertical dashed line in (b)). (b) Input (magenta) and output (black) grid-tuning index as a function of the input-tuning strength β. Solid lines depict median values, shaded areas span from the first to the third quartile of the distribution. The vertical dashed line indicates the input-tuning strength β = 0.35 that was used to learn the recurrent connections. (c) Grid-amplification index as a function of the input-tuning strength β. The grid-amplification index is the ratio between output and input grid-tuning indexes. See Section 4 for further details and Table 1 for parameter values [Color figure can be viewed at wileyonlinelibrary.com]

that are lower than the ones experienced during learning (β = 0.35, dashed lines in Figure 4b,c). Therefore, the recurrent network can generalize across a wide range of input-tuning strengths (see also Figure A4b in Appendix A for similar results in the one-dimensional model).

In a second set of simulations, we study how the input tuning affects the learning of the recurrent connections (Figure 5). To this end, we train the network with different input-tuning strengths and check whether a structure emerges in the synaptic weights. As expected, the higher the input tuning the clearer the connectivity structure, that is, cells with similar grid phases develop strong recurrent connections (Figure 5a). We quantify this effect by means of the *connectivity-tuning index*, which measures the amount of clustering of the synaptic weights when they are sorted according to grid phase (see Section 4.6, for details). Figure 5b shows the connectivity-tuning index as a function of the input-tuning strength β during learning. The index steeply increases for $0.2 < \beta < 0.4$ and saturates at high values for $\beta > 0.6$.

Finally, we assess the network's amplification performance with such learned connectivities (Figure 5c). For sufficiently strong input-tuning strength during learning (e.g., $\beta > 0.3$), the resulting networks reach up to a tenfold amplification of the feedforward grids. Note that because the output grid-tuning index saturates at about 0.6, the grid-amplification index decays for large input-tuning strengths β after learning (Figure 5c); see also Figure 4c for a similar effect.

In summary, the recurrent network can strongly amplify grid-cell activity for a wide range of input-tuning strengths, provided that the input tuning during learning was sufficiently strong.

2.4 | Effects of noise correlations on amplification and learning

So far we have studied the amplification of grid-cell activity in a network of noisy grid cells where the input noise was *uncorrelated* across neurons. This was a favorable scenario for amplification because

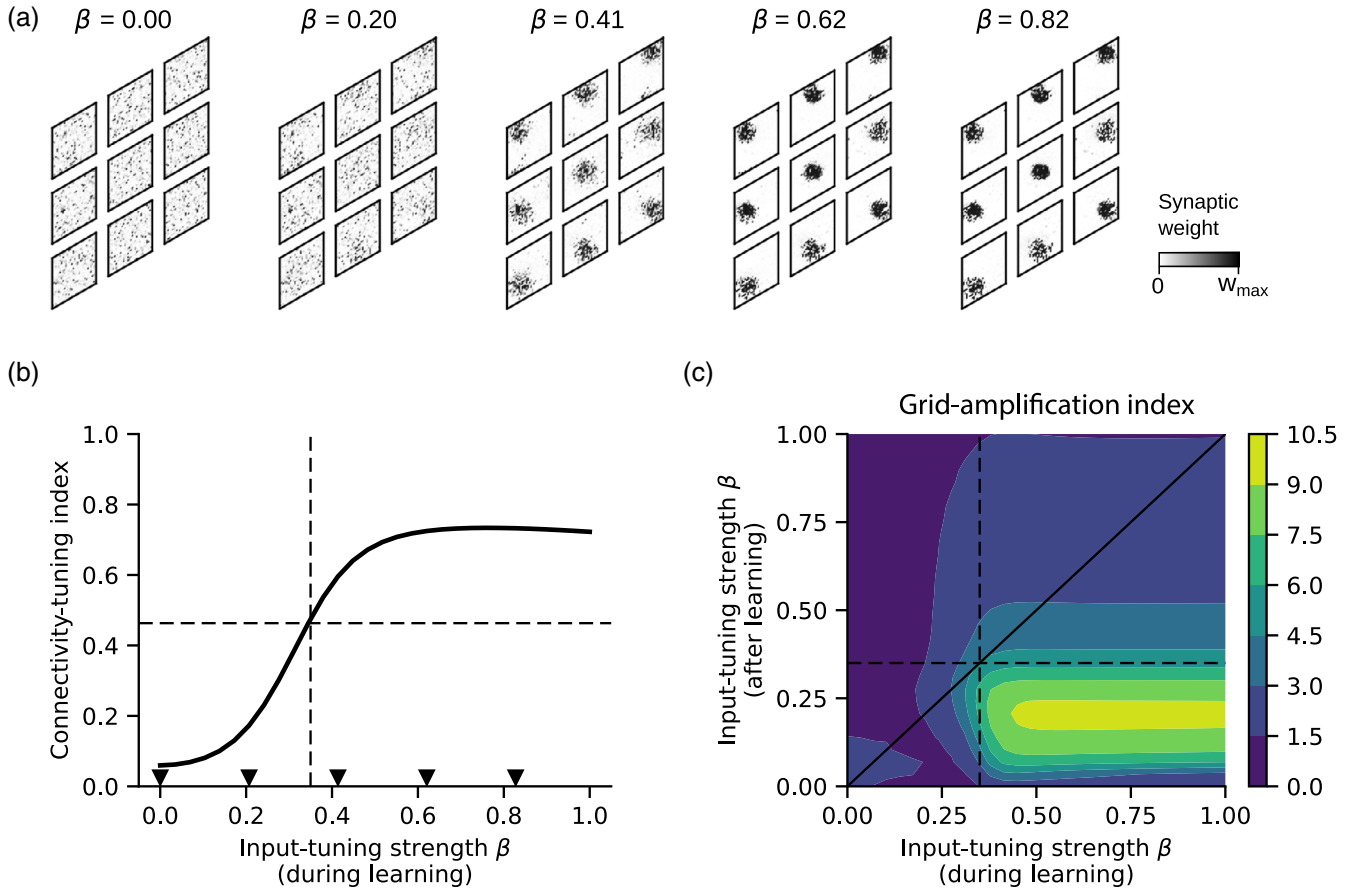

FIGURE 5 Effects of input tuning on learning. (a) Recurrent excitatory connectivity learned with five example input-tuning strengths β (see also triangles in (b)). For each tuning strength, the synaptic weights to nine (out of 900) example excitatory cells are shown (small rhombi). Nearby pixels correspond to inputs with similar grid phases (see also Figure 1b). (b) Connectivity-tuning index as a function of the input-tuning strength during learning. The connectivity-tuning index measures the amplitude of the first harmonic of the synaptic weights in phase space (see Section 4.6, for details). The dashed lines denote the default input-tuning strength (β = 0.35, Figure 1b) and the resulting connectivity-tuning index (≈0.48). (c) Grid-amplification index as a function of the input-tuning strength during and after learning (mean across neurons). The dashed lines denote default parameter values. See Section 4 for further details and Table 1 for parameter values [Color figure can be viewed at wileyonlinelibrary.com]

uncorrelated noise can be easily averaged out by recurrent dynamics. In the real biological system, however, correlations across neurons may exist. In fact, we hypothesized that noisy grids initially emerge by summation of spatially tuned inputs (e.g., D'Albis & Kempter, 2017; Kropff & Treves, 2008), and shared feedforward input could generate correlations across neurons.

To study how input correlations impact amplification and learning, in what follows we generate feedforward inputs by corrupting regular grids with correlated spatial noise. Crucially, we assume that noise correlations depend on the spatial tuning of the cells, that is, cells with similar preferred phases have strong noise correlations. This is a reasonable assumption because cells with similar preferred phases are likely to share a large fraction of feedforward inputs, and the noise in these shared inputs is identical. Formally, the noise autocorrelation at the population level (across neurons) is assumed to be a von Mises function of the phase difference $\Delta\vec{\varphi}$ between two cells: it peaks at $\Delta\vec{\varphi} = 0$ and decays with spread $\sigma_{\vec{\varphi}} > 0$ for larger values of $\Delta\vec{\varphi}$ (see Section 4.2 for details). The noise-correlation length $\sigma_{\vec{\varphi}}$ controls the fraction of shared noise that the network receives and it could mirror the degree of convergent connectivity at the feedforward input.

Figure 6a1 shows five examples of the population feedforward input with increasing values of the correlation length $\sigma_{\vec{\varphi}}$. At the population level, each rhomboidal map shows the firing rate of all excitatory neurons in the network for a particular position of the virtual rat

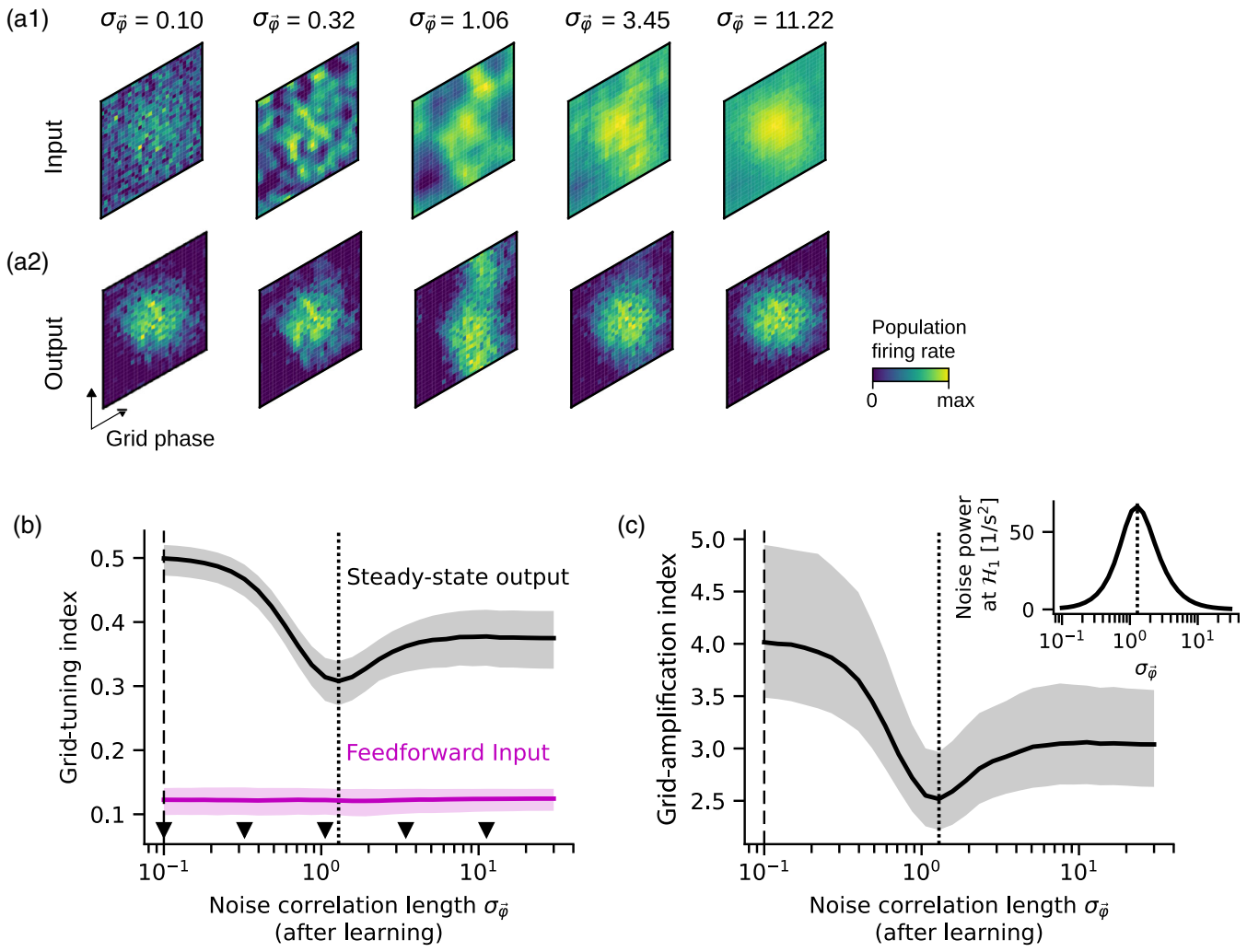

FIGURE 6 Effects of input noise correlations on grid-pattern amplification. (a) Example population feedforward inputs (a1) and population steady-state outputs (a2) for five input-noise correlation lengths $\sigma_{\vec{\varphi}}$ (see also triangles in (b)). Each firing-rate map depicts the activity of all excitatory neurons in the network (sorted by grid phase) for a particular position of the virtual rat (here: center of the arena). (b) Input (magenta) and output (black) grid-tuning index as a function of $\sigma_{\vec{\varphi}}$. Output grid-tuning indexes are computed at the steady-state of the recurrent dynamics with fixed recurrent connectivity, as shown in Figure 1b2. The recurrent connectivity was learned with effectively uncorrelated noise across neurons ($\sigma_{\vec{\varphi}} = 0.1$, vertical dashed line). Simulations were repeated for 10 distinct realizations of the input noise. The results are pooled across realizations and across neurons. Solid lines depict median values, shaded areas span from the first to the third quartile of the distribution. (c) Grid-amplification index as a function of $\sigma_{\vec{\varphi}}$. The dotted lines indicate the value of $\sigma_{\vec{\varphi}} \approx 1.25$ for which the noise power at the first harmonic in phase space is maximal (inset). Inset: Noise power at the first harmonic $\mathcal{H}_1$ as a function of $\sigma_{\vec{\varphi}}$. See Section 4 for further details and Table 1 for parameter values [Color figure can be viewed at wileyonlinelibrary.com]

in the environment (here: center of the arena), and neurons are sorted according their preferred grid phase. For $\sigma_{\vec{\varphi}} = 0.1$ (Figure 6a1, top left), the noise is effectively uncorrelated across neurons, because noise correlations are shorter than the phase-sampling interval $2\pi/\sqrt{N_E} \approx 0.2$. In this case, the population activity resembles a noisy bump (generated by the weak grid signal) corrupted by salt-and-pepper-like noise. For increasing values of $\sigma_{\vec{\varphi}}$, the noise is smoother and smoother at the population level, meaning that larger and larger groups of neurons with close-by phases receive common input. For large values of $\sigma_{\vec{\varphi}}$ (e.g., $\sigma_{\vec{\varphi}} = 11.22$ in Figure 6a1, top right), the noise approaches a constant at the population level. Note that a noisy bump of activity is visible in the centers of the rhomboidal maps for both small and large correlation lengths, but disappears at intermediate levels.

Figure 6a2 shows the steady-state output of the network for the inputs in Figure 6a1. A clear bump of activity emerges at the population output for all correlation lengths $\sigma_{\vec{\varphi}}$ (see also Figure A2 in Appendix B for a similar effect in the reduced one-dimensional model). However, the bump is distorted for intermediate correlation lengths (e.g., $\sigma_{\vec{\varphi}} = 1.06$). This result suggests that the network's amplification performance is a non-monotonic function of the noise correlation length $\sigma_{\vec{\varphi}}$. In fact, when we compute the median grid-tuning index across all excitatory cells in the network, we find that the index has a global minimum for $\sigma_{\vec{\varphi}} \approx 1.25$ at the steady-state output (Figure 6b, black), but remains approximately constant at the feedforward input (Figure 6b, magenta). Accordingly, the grid-amplification index is a non-monotonic function of $\sigma_{\vec{\varphi}}$ and reaches a minimum for $\sigma_{\vec{\varphi}} \approx 1.25$ (Figure 6c, see also Figure A5 in Appendix A for a similar effect in the reduced one-dimensional model).

This result can be explained as follows. The structured recurrent connectivity that emerged after learning effectively amplifies the first harmonic of the population input (see also mathematical results in Appendix A). This is because the recurrent connections reinforce the activity of cells with similar phases, which form an activity bump at the population level (Figure 6a). As a result, the amplification performances depend on the noise power at this first harmonic $\mathscr{H}_1$, i.e., the stronger the noise power at harmonic $\mathscr{H}_1$ the worse the amplification. The inset of Figure 6c shows the noise power at harmonic $\mathscr{H}_1$ as a function of the noise correlation length $\sigma_{\vec{\varphi}}$. For small values of $\sigma_{\vec{\varphi}}$, the noise power is evenly distributed across all frequencies and the power at $\mathscr{H}_1$ is small. As $\sigma_{\vec{\varphi}}$ increases, the noise power shifts towards the low frequencies and the power at $\mathscr{H}_1$ increases. For $\sigma_{\vec{\varphi}} \approx 1.25$ the noise power at the first harmonic $\mathscr{H}_1$ is maximal (dotted lines), and the worst amplification performances are obtained. Finally, for large values of $\sigma_{\vec{\varphi}}$, the noise power at $\mathscr{H}_1$ decays because only the zeroth harmonic survives.

So far in this section, we have explored how input noise correlations affect grid-pattern amplification for a fixed recurrent connectivity. We now study how noise correlations across neurons affect the learning of the recurrent connections (Figure 7). Figure 7a shows examples of the recurrent excitatory weights obtained with different noise correlation lengths $\sigma_{\vec{\varphi}}$ during learning. A phase-dependent connectivity structure arises for all values of $\sigma_{\vec{\varphi}}$, but the structure is clearest for intermediate correlation lengths (e.g., $\sigma_{\vec{\varphi}} = 1.06$ in Figure 7a). Accordingly, the connectivity-tuning index peaks for $\sigma_{\vec{\varphi}} \approx 1.25$ (Figure 7b, black line). However, at the same correlation length, we have previously found that the network's amplification performance is minimal after learning (Figure 6c).

We generalize these findings in Figure 7c, which shows the grid-amplification index as a function of the noise-correlation length both during and after learning. We confirm that grid-amplification is lowest for intermediate correlation lengths after learning. Interestingly, however, we also find that input-noise correlations are favorable for learning.

To understand why noise correlations promote structure formation, recall that we have assumed a noise model where correlations are highest among cells with similar phases. In this scenario, noise co-activates cells with close-by phases and, as a result, the connectivity between those cells is reinforced. This suggests that a structured recurrent connectivity could emerge even in the absence of a grid signal during learning. We test this hypothesis by setting the input-tuning strength $\beta = 0$ during learning. As expected, we find that the connectivity-tuning index becomes large for a wide range of correlation lengths $\sigma_{\vec{\varphi}}$ with a peak at $\sigma_{\vec{\varphi}} \approx 1.25$ (Figure 7b, gray line).

Although this result appears counter-intuitive at first, it can be easily explained as follows. Consider any two excitatory cells in the network. During an initial learning phase (not modeled here), structure formation occurs at their feedforward connections and noisy grid patterns emerge. If these two grid patterns have similar phases they may also share common feedforward inputs. In this case, the feedforward connectivity (which is fixed across network states) generates activity correlations that promote future co-activation of the same cells. As a result, the two cells can form recurrent connections even when sensory signals are turned OFF, for example, during sleep.

In summary, we find that noise correlations across neurons are detrimental for grid-pattern amplification, and the worst amplification performance is obtained when the noise correlation length is comparable to the size of an activity bump at the population level. On the other hand, noise correlations promote the emergence of a structured recurrent connectivity and a grid signal may not even be necessary for such learning.

3 | DISCUSSION

Recent experimental findings indicate that entorhinal grid cells are embedded in highly recurrent excitatory circuits (Fuchs et al., 2016; Gardner et al., 2019; Schmidt et al., 2017; Trettel et al., 2019; Winterer et al., 2017). We proposed that such recurrent connections could serve to amplify grid-cell tuning, and we supported this hypothesis with a computational model. Assuming that weak, noisy grids are initially generated by a feedforward mechanism (e.g., D'Albis & Kempter, 2017; Kropff & Treves, 2008), we showed that Hebbian synaptic plasticity leads to a tuning of the feedback excitatory connections that amplify periodic patterns for a wide range of inputs. We quantified this amplification by introducing a novel, Fourier-based

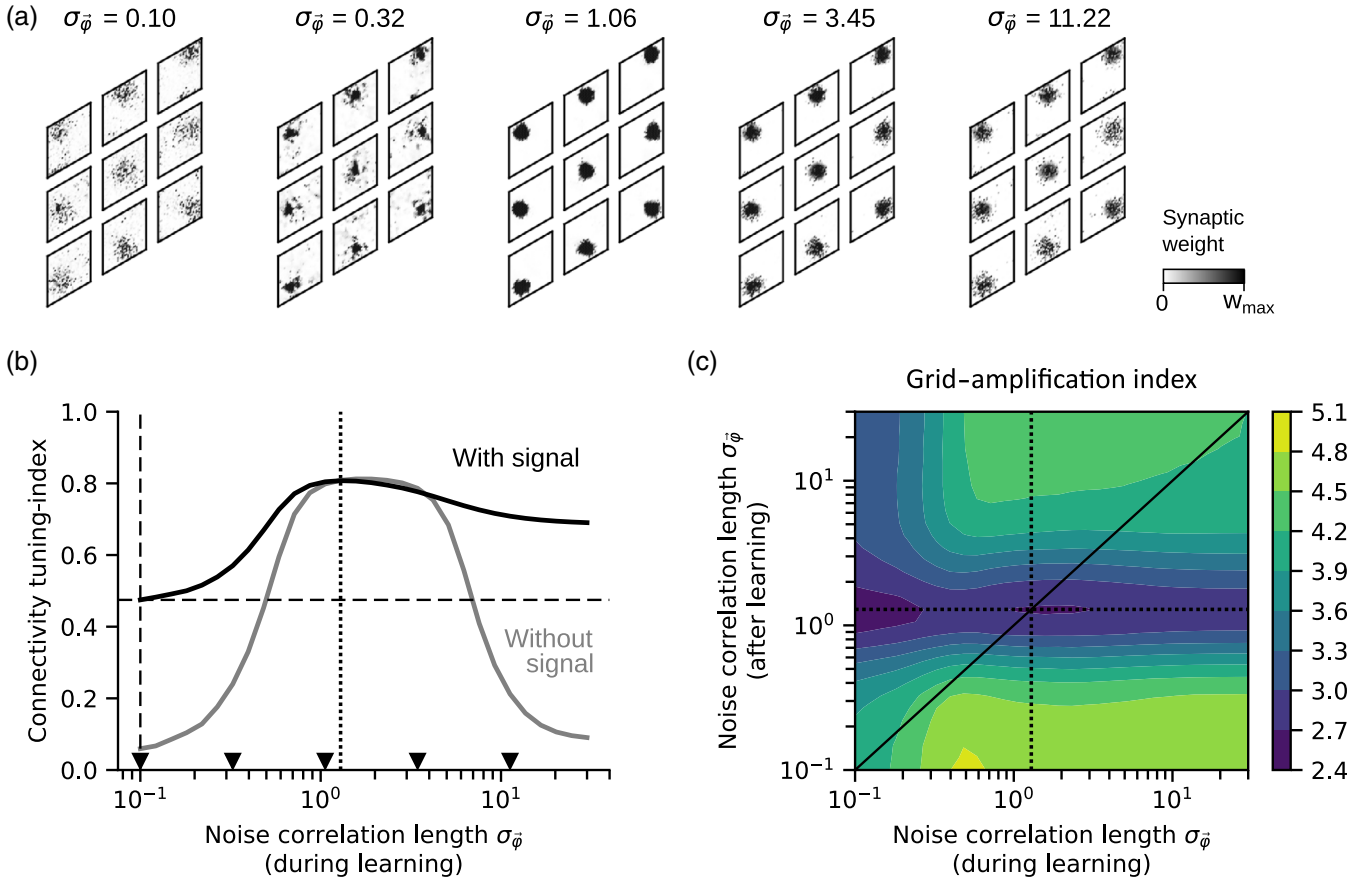

FIGURE 7 Effects of input noise correlations on learning. (a) Five examples of the learned recurrent excitatory connectivity as a function of the noise correlation length $\sigma_{\vec{\varphi}}$. (b) Connectivity-tuning index as a function of $\sigma_{\vec{\varphi}}$ with signal (black, input-tuning strength β = 0.35) and without signal (gray, β = 0). The connectivity-tuning index measures the amplitude of the first harmonic of the synaptic weights in phase space. The dashed lines denote the default correlation length ($\sigma_{\vec{\varphi}}$ = 0.1, Figure 1b) and the corresponding connectivity-tuning index (≈0.48). The dotted line indicates the value of $\sigma_{\vec{\varphi}} \approx 1.25$ for which the noise power at the first harmonic is maximal (Figure 6c, inset). (c) Grid-amplification index as a function of $\sigma_{\vec{\varphi}}$ during and after learning. The index is computed for 10 distinct realizations of the input noise. The results are pooled across realizations and across neurons. The heat map shows the mean of the distribution. The dotted lines indicate the value of $\sigma_{\vec{\varphi}} \approx 1.25$ for which the noise power at the first harmonic is maximal. See Section 4 for further details and Table 1 for parameter values [Color figure can be viewed at wileyonlinelibrary.com]

measure for the periodicity of grid-cell patterns. In our model, inhibitory neurons displayed a very weak grid tuning, and amplification was fast enough to occur within a single cycle of the theta rhythm. We also demonstrated that the learned excitatory connectivity could support attractor dynamics, that is, it could sustain a localized bump of activity at the population level even in the absence of feedforward tuning. Finally, we found that noise correlations across neurons (e.g., due to shared input) hinder grid-pattern amplification during active exploration, but promote structure formation during learning.

3.1 | Origin of grid patterns and grid modules

A central assumption of our work is that grid-cell activity originates via a feedforward mechanism prior to the development of the recurrent connections (e.g., Castro & Aguiar, 2014; D'Albis & Kempter, 2017; Dordek et al., 2016; Mhatre et al., 2012; Monsalve-Mercado & Leibold, 2017; Stepanyuk, 2015; Weber & Sprekeler, 2018). Here, we do not model such a feedforward mechanism explicitly, but we posit that feedforward connections from spatially selective inputs (e.g., place cells or spatially irregular cells) have been already tuned to produce noisy grid patterns. Such noise has been introduced in the model to account for spatial irregularities resulting from uneven sensory coverage during learning and/or distortions due to spatially irregular inputs (Diehl et al., 2017). In fact, all grid-cell models based on synaptic plasticity and experience were shown to produce spatial irregularities (e.g., D'Albis & Kempter, 2017; Dordek et al., 2016; Monsalve-Mercado & Leibold, 2017; Weber & Sprekeler, 2018), and empirically observed grid patterns are often distorted or irregular, particularly in young developing animals (Langston et al., 2010; Wills et al., 2010).

We assumed that recurrent connections develop among co-modular grids, that is, grids with similar spacing and orientation but distributed spatial phases. Consistently with this assumption, recurrent excitatory connectivity decays sharply with somatic distance

(Holmgren, Harkany, Svennenfors, & Zilberter, 2003; Perin, Berger, & Markram, 2011; Stepanyants & Chklovskii, 2005), and anatomically nearby grid cells are co-modular (Hafting et al., 2005; Stensola et al., 2012). The mechanisms underlying the formation of such modules are still debated, but theoretical work suggests that recurrent excitatory coupling could also support this function (Urdapilleta et al., 2017). In fact, Urdapilleta et al., 2017 have shown that a feedforward model where grid scale is controlled by a smooth gradient of adaptation time constants can generate distinct modules at discrete spatial scales. In their model, scale modularity and grid alignment were achieved via recurrent coupling and conjunctive head-direction selectivity (see also Si, Kropff, & Treves, 2012; Si & Treves, 2013)—although it was not systematically tested whether grid phases were uniformly distributed after learning. See also (Kang & Balasubramanian, 2019) for an alternative explanation of grid-cell modularity in the context of CAN models.

The goal of the present study was to model a learning process that occurs within a single grid-cell sub-network, after a modular structure has already emerged. It remains to be investigated to which extent our results are robust to non-uniform distributions of grid phases and broader distributions of grid orientations.

Our modeling assumptions are also supported by the finding that grid cells in MEC layer II are physically clustered within modules (Gu et al., 2018; Heys et al., 2014; Kitamura et al., 2014; Naumann et al., 2016; Naumann, Preston-Ferrer, Brecht, & Burgalossi, 2018; Ray et al., 2014)—a configuration that is suggestive of a high recurrent connectivity at the microcircuit level. Notably, the network size considered in our amplification model roughly matches the number of cells found in a typical pyramidal-cell patch of the human MEC (~900 cells; Naumann et al., 2016).

3.2 | Synaptic plasticity and learning

We propose that feedback connections between grid cells become structured through synaptic plasticity. This is in line with synaptic long-term potentiation and depression being reported in the entorhinal cortex (Alonso, De Curtis, & Llinas, 1990; De Curtis & Llinas, 1993; Solger, Wozny, Manahan-Vaughan, & Behr, 2004; Yang et al., 2004; Yun, Mook-Jung, & Jung, 2002; Zhou, Acker, Netoff, Sen, & White, 2005); but see also (Deng & Lei, 2007). In our model, a structured recurrent connectivity emerges after about 10–20 min of a virtual rat continuously exploring an environment. However, because the learning rate is underconstrained in our model (and we do not consider stochastic spiking dynamics), we cannot predict the actual time needed for learning.

To avoid positive-feedback loops between activity and plasticity, we turned OFF the recurrent dynamics during learning and disabled synaptic plasticity during amplification. At this regard, we propose that neuromodulators, such as acetylcholine, may differentially regulate activity and plasticity according to the behavioral state of the animal, that is, recurrent synapses could be active (but not plastic) during active exploration, and plastic (but not active) during sleep (see for example, Hasselmo, 2006).

The hypothesis that recurrent connections could be learned during sleep is supported by our finding that noise correlations across neurons are sufficient to generate a phase-specific recurrent connectivity (which leads to amplification) even in the absence of grid tuning at the feedforward input (Figure 7b). This is because we have assumed that noise correlations are stronger between cells with similar feedforward tuning (grid phase in our case)—a scenario that has been observed in sensory cortices (Kohn & Smith, 2005; Lampl, Reichova, & Ferster, 1999). As a result, even a random activation of the feedforward inputs could co-activate cells with similar tuning and reinforce their connections. In summary, once the feedforward connections are in place, recurrent synapses could develop independently of grid-cell input.

3.3 | The role of inhibition in grid-pattern amplification

We simulated the amplification of grid-cell activity in a recurrent network comprising both excitatory and inhibitory neurons. We assumed that inhibition was unstructured, that is, a single interneuron received input from (and provided output to) a random set of excitatory cells. This scenario is consistent with experimental data on PV^+ interneurons in the MEC, which were found to connect to grid cells in a phase-unspecific manner (Buetfering et al., 2014). As a result, inhibitory neurons in our model display a very weak spatial tuning, which is consistent with experimental data (Buetfering et al., 2014).

We propose that inhibition provides a baseline shift to the firing rates of the excitatory cells, reducing both in-field and out-of-field activity. In our simulations, such a baseline shift leads to sharper grid tuning at the output. These results are consistent with experiments showing that grid cells exhibit higher firing rates and broader grid tuning after inactivation of PV^+ interneurons (Buetfering et al., 2014; Miao et al., 2017).

Due to the random inhibitory connectivity, our network operates in a Hebbian (or normal) amplification regime, meaning that a tradeoff exists between the speed of a network's response and the amount of amplification that can be reached—a phenomenon termed "Hebbian slowing" (Murphy & Miller, 2009). Yet considering typical grid-spatial scales, exploration speeds, and network-integration time constants, we showed that grid-cell activity could be considerably amplified in a short time frame, for example, within a single cycle of the theta rhythm (Figure 2).

3.4 | Attractor dynamics in the absence of input tuning

To outline the relationship between our model and CAN networks for grid-cell activity, we tested whether the learned recurrent connectivity could support attractor dynamics without spatially tuned feedforward inputs. We found that the network maintains a localized activity bump even without input tuning, which is a signature of attractor dynamics (Figure 3). However, the network exhibits only a

few discrete attractors rather than a continuum of attractor states as in an idealized CAN.

This result can be explained by the fact that the recurrent excitatory connectivity that emerges via Hebbian learning is noisy (see Figure 1b2 for an example) and departs considerably from the smooth bell-shaped profiles typically assumed in CANs. Moreover, random connectivity with inhibitory neurons introduces further quenched disorder that generates local minima in the network's energy landscape (Itskov, Hansel, & Tsodyks, 2011; Kilpatrick, Ermentrout, & Doiron, 2013; Zhang, 1996; Zhong, Lu, Schwab, & Murugan, 2020). If the signal-strength during learning is increased (as in Figure 5a), the learned excitatory connectivity is less noisy and the number of attractor states slightly increases. However, even with full signal-strength during learning ($\beta = 1$), we find that the network exhibits a low number of discrete attractors.

Further research is needed to find out whether a larger number or even a continuum of attractors could be obtained by modifications of the synaptic plasticity rule, for example, using a less competitive rule that leads to a broader distribution of synaptic efficacies and therefore a smoother bump in weight space.

3.5 | The functional role of recurrent connectivity in the MEC

Recurrent dynamics is at the core of CAN models for the origin of grid-cell activity (e.g., Burak & Fiete, 2009; Fuhs & Touretzky, 2006; Guanella et al., 2007; McNaughton et al., 2006). In these models, however, feedback projections generate spatial selectivity ab initio rather than "merely" amplifying feedforward tuning. In the following, we propose a conceptual framework in which CAN and amplification models can be reconciled.

We hypothesize that during development weakly periodic grid patterns emerge from a feedforward process driven by spatially selective inputs and experience. Shortly after the onset of this learning phase, activity-dependent synaptic plasticity connects cells with similar grid phases and generates a structured recurrent connectivity alike to the one obtained in our simulations. We have shown that such a recurrent connectivity can amplify grids when the feedforward input is noisy and can maintain a localized bump of activity at the population level when the feedforward input is untuned. However, such a network is not yet capable of path integration.

The same network, however, could now learn to path integrate by developing synaptic connections with self-motion inputs (e.g., speed and head-direction cells) under the supervision of feedforward sensory signals (see, for example, Stringer, Trappenberg, Rolls, & De Araujo, 2002; Hahnloser, 2003; Widloski & Fiete, 2014). As a result, the fully mature circuit could operate in two different modes: on the one hand, it could amplify feedforward sensory information when this is available; on the other hand it could sustain grid patterns by integrating self-motion signals when no other external sensory cue can be used.

A computational model in which a grid-cell CAN is learned from spatially selective inputs has been proposed by Widloski and Fiete (2014). In this model, however, the velocity-integration gain did not match the feedforward inputs, that is, the dynamics of the mature network was uncoupled from the external sensory signals. A challenge for future research is to develop a model in which spatial and velocity-modulated signals work in a synergistic manner to maintain reliable spatial representations across sensory conditions.

3.6 | Predictions and conclusions

The central prediction of our work is that Hebbian synaptic plasticity generates a phase-specific recurrent connectivity between grid cells after a weak grid tuning has already emerged at the feedforward input. Indirect experimental evidence suggests that such a structured recurrent connectivity is indeed present in mature grid-cell networks (Dunn et al., 2015; Gardner et al., 2019; Tocker et al., 2015; Trettel et al., 2019; Yoon et al., 2013) but whether this connectivity emerges through activity-dependent processes is still unclear.

A similar question has been addressed in visual cortex. To study the emergence of functionally organized cortical circuits, Ko et al., (2013) characterized the tuning curves of nearby cells in V1 through two-photon optical imaging in vivo, and subsequently tested for connectivity patterns between the same cells using whole-cell recordings in vitro. By repeating the experiment with animals at different developmental stages and visual experience, the authors found that local recurrent connectivity in V1 extensively reorganized to match the orientation tuning inherited from the thalamus (Ko et al., 2013). We suggest that an analogous experimental framework could be used to track the maturation and tuning of recurrent connectivity in the MEC.

We further predict that feedback excitatory connections amplify grid patterns, but do not generate them in the first place. This hypothesis could be tested by silencing the output activity of a recurrently connected grid-cell population while recording excitatory post-synaptic currents (EPSC) at the feedforward input. We predict that the feedforward EPSCs shall be already weakly grid tuned. Such an approach has been proven successful in demonstrating recurrent amplification in visual cortex (Lien & Scanziani, 2013). However, isolating feedforward and recurrent excitation in sub-populations of entorhinal neurons may be more difficult than in visual pathways.

Finally, we propose that grid-cell patterns are initially and predominantly sensory-based representations, whereas path-integration capabilities develop in a later stage during development. We therefore predict that path integration shall be disrupted if animals were sensory deprived for extensive time periods during development. Additionally, selectively inactivating speed or head-direction cells in the MEC of young animals shall impair path-integration capabilities but spare the periodic tuning of entorhinal grid cells.

4 | MATERIALS AND METHODS

In this section, we describe the grid-pattern amplification model in details. Parameter values are summarized in Table 1.

TABLE 1 Parameters of the two-dimensional grid-amplification model

Neural activity		
N_E	900	Number of excitatory neurons
N_I	225	Number of inhibitory neurons
τ	10 ms	Network integration time constant
r_{max}	100 s^{-1}	Maximal firing rate
f_{EE}	0.1	Connectivity rate of the $E \to E$ connection
f_{EI}	0.4	Connectivity rate of the $I \to E$ connection
f_{IE}	0.4	Connectivity rate of the $E \to I$ connection
f_{II}	0.4	Connectivity rate of the $I \to I$ connection
w_{tot}^{EE}	2	Total synaptic strength of the $E \to E$ connection
w_{tot}^{EI}	0.4	Total synaptic strength of the $I \to E$ connection
w_{tot}^{IE}	10	Total synaptic strength of the $E \to I$ connection
w_{tot}^{II}	1	Total synaptic strength of the $I \to I$ connection
Input spatial tuning		
r_{av}	5 s^{-1}	Average input rate in the arena
β	0.35	Input-tuning strength
μ_T	0.5 m	Average grid spacing of the inputs grids
σ_T	0.03 m	Standard deviation of the input-grid spacings
μ_γ	0	Average grid orientation of the input grids
σ_γ	0.03	Standard deviation of the input-grid orientations
$\sigma_{\vec{\varphi}}$	0.1	Noise correlation length across neurons
$\sigma_{\vec{x}}$	0.3	Noise correlation length in space
Synaptic plasticity		
η	2×10^{-5}	Learning rate
Spatial exploration		
L	2 m	Side-length of the arena
v	0.25 m/s	Running speed of the virtual rat
σ_θ	0.7	Standard deviation of running directions
Derived quantities		
w_{max}	≈0.02	Maximal synaptic strength of the $E \to E$ connections

Note: The table reports the default parameter values for all numerical simulations of the 2D grid-amplification model.

4.1 | Model of neural activity

We model a recurrent network comprising a population of N_E excitatory neurons with firing rates $\{r_i^E : i = 1,2,...,N_E\}$ and a population of N_I inhibitory neurons with firing rates $\{r_i^I : i = 1,2,...,N_I\}$. The two populations are recurrently connected locally. The external drive to the network is provided by spatially tuned feedforward inputs $\{h_i : i = 1, 2, ..., N_E\}$ that project exclusively to the excitatory population (Figure 1a).

The network activity follows a classical firing-rate description. The firing rates of the excitatory neurons are

$$\tau \frac{dr_i^E(t)}{dt} := -r_i^E(t) + F\left(h_i(t) + \sum_{j=1}^{N_E} w_{ij}^{EE} r_j^E(t) - \sum_{j=1}^{N_I} w_{ij}^{EI} r_j^I(t)\right) \quad (1)$$

where $\tau > 0$ is the integration time constant of the network, $h_i \geq 0$ is the total feedforward input to neuron i, $w_{ij}^{EE} \geq 0$ is the synaptic weight from excitatory neuron j to excitatory neuron i, and $w_{ij}^{EI} \geq 0$ is the synaptic weight from inhibitory neuron j to excitatory neuron i. The activation function

$$F(x) := \begin{cases} r_{max} \tanh(x/r_{max}) & \text{for } x > 0 \\ 0 & \text{otherwise} \end{cases} \quad (2)$$

bounds the firing rates between 0 and $r_{max} > 0$. Similarly, the firing rates of the inhibitory neurons are

$$\tau \frac{dr_i^I(t)}{dt} := -r_i^I(t) + F\left(\sum_{j=1}^{N_E} w_{ij}^{IE} r_j^E(t) - \sum_{j=1}^{N_I} w_{ij}^{II} r_j^I(t)\right) \quad (3)$$

where $w_{ij}^{IE} \geq 0$ is the synaptic weight from excitatory neuron j to inhibitory neuron i and $w_{ij}^{II} \geq 0$ is the synaptic weight from inhibitory neuron j to inhibitory neuron i. Note that in the simulations of Figure 2b,c, we introduce theta modulation by multiplying the feedforward inputs h_i in Equation (1) by the function

$$\theta(t) := [\cos(2\pi f_\theta t) + 1]/2 \quad (4)$$

where $f_\theta = 8$ Hz is the frequency of the theta rhythm.

The synaptic connectivity is sparse and initially random, that is, each presynaptic neuron is connected to a random subset of postsynaptic neurons in the target neuronal population. The connectivity rates are set by the parameters f_{EE}, f_{EI}, f_{IE}, and f_{II}, where f_{BA} is the connectivity rate from neuronal population A to neural population B. Similarly, the total connection strengths are set by the parameters w_{tot}^{EE}, w_{tot}^{EI}, w_{tot}^{IE}, and w_{tot}^{II}. The initial synaptic weights are set by dividing the total connection strength by the number of connected neurons.

4.2 | Model of input spatial tuning

The feedforward input h_i to excitatory neuron i = 1, 2, ..., N_E is tuned as a function of the location $\vec{x}$ of a virtual rat in the environment:

$$h_i := h\left(\vec{\varphi}_i, \vec{x}\right) := \left[\beta g\left(\vec{\varphi}_i, \vec{x}\right) + (1-\beta)\xi\left(\vec{\varphi}_i, \vec{x}\right) + H\right]_+ \quad (5)$$

where $g\left(\vec{\varphi}_i, \vec{x}\right)$ is a spatially periodic grid signal with phase $\vec{\varphi}_i$, and $\xi\left(\vec{\varphi}_i, \vec{x}\right)$ is a blanket of spatial noise impinging to neuron $\vec{\varphi}_i$. The

parameter $0 \le \beta \le 1$ sets the input-tuning strength, H is a constant, and the function $[x]_+$ is a static non linearity, that is, $[x]_+ = x$ if $x > 0$, and $[x]_+ = 0$ otherwise. The value of H is determined numerically such that the total input $\sum_{i,\vec{x}} h\left(\vec{\varphi}_i, \vec{x}\right)$ remains constant for each input-tuning strength β.

4.2.1 | Grid signal

The grid signal $g\left(\vec{\varphi}_i, \vec{x}\right)$ is obtained by superimposing circularly symmetric Gaussian functions $G_i\left(\vec{x}\right) := \exp\left(-\left|\vec{x}\right|^2/(2\sigma_i^2)\right)$ at the vertices of a periodic triangular lattice. Formally, neuron i has grid vertices

$$\vec{p}_{ab}^{(i)} := \frac{T_i}{2\pi}\left(a\vec{u}_1 + b\vec{u}_2 + \vec{\varphi}_i\right) \quad \text{with} \quad a,b \in \mathbb{Z} \tag{6}$$

where T_i is the grid spacing and

$$\vec{u}_1 := 2\pi\begin{bmatrix}\cos(\pi/6+\gamma_i)\\ \sin(\pi/6+\gamma_i)\end{bmatrix} \quad \text{and} \quad \vec{u}_2 := 2\pi\begin{bmatrix}\cos(\pi/2+\gamma_i)\\ \sin(\pi/2+\gamma_i)\end{bmatrix} \tag{7}$$

are the unit vectors of a triangular lattice with period 2π and orientation γ_i. The grid phases $\vec{\varphi}_i$ are evenly sampled in the rhombus spanned by the unit vectors $\vec{u}_1$ and $\vec{u}_2$. The grid spacings T_i are normally distributed with mean μ_T and standard deviation σ_T. The grid orientations γ_i are normally distributed with mean 0 and standard deviation σ_γ. The field sizes $\sigma_i := T_i/3$ are proportional to the grid spacings T_i. The grid signal is sampled within a square enclosure of side length L.

4.2.2 | Spatial noise

The noise term $\xi\left(\vec{\varphi}_i, \vec{x}\right)$ in Equation (5) is a stationary Gaussian random field with zero mean and autocorrelation $C\left(\Delta\vec{\varphi}, \Delta\vec{x}\right)$, where $\Delta\vec{\varphi}$ is the difference between two grid phases and $\Delta\vec{x}$ is the difference between two spatial locations. We assume the following noise-correlation structure:

$$C\left(\Delta\vec{\varphi}, \Delta\vec{x}\right) = KC_{\vec{\varphi}}\left(\Delta\vec{\varphi}\right)C_{\vec{x}}\left(\Delta\vec{x}\right) \tag{8}$$

where $C_{\vec{\varphi}}$ sets the noise correlations across neurons, $C_{\vec{x}}$ sets the noise correlations in space, and K scales the noise variance. We define

$$C_{\vec{\varphi}}\left(\Delta\vec{\varphi}\right) := \exp\left(\frac{\sum_{n=0}^{2}\cos\left(\Delta\vec{\varphi}\cdot\vec{k}_n\right) - 3}{\sigma_{\vec{\varphi}}^2}\right) \quad \text{with} \quad \vec{k}_n := \begin{bmatrix}\cos(n\pi/3)\\ \sin(n\pi/3)\end{bmatrix} \tag{9}$$

where $\sigma_\varphi > 0$ sets the noise-correlation length across neurons. Similarly, we define

$$C_{\vec{x}}\left(\Delta\vec{x}\right) := \exp\left(\frac{\sum_{n=0}^{1}\cos\left(\Delta\vec{x}\cdot\vec{m}_n\right) - 2}{\sigma_{\vec{x}}^2}\right) \quad \text{with} \quad \vec{m}_n := \frac{2\pi}{L}\begin{bmatrix}\cos(n\pi/2)\\ \sin(n\pi/2)\end{bmatrix} \tag{10}$$

where $\sigma_{\vec{x}} > 0$ sets the noise-correlation length in space. Note that the noise variance $C\left(\vec{0}, \vec{0}\right) = K$ is fixed and independent of the parameters $\sigma_{\vec{\varphi}}$ and $\sigma_{\vec{x}}$. We set the noise variance al to the variance of the grid signal, that is, $K = \left\langle g\left(\vec{\varphi}, \vec{x}\right)^2\right\rangle_{\vec{\varphi},\vec{x}} - \left\langle g\left(\vec{\varphi}, \vec{x}\right)\right\rangle_{\vec{\varphi},\vec{x}}^2$.

4.2.3 | Experiments in the absence of input tuning

In Figure 3 we probe the network dynamics with spatially untuned feedforward input. In the simulations of Figure 3a,b, in the untuned condition, the feedforward input is set to a constant value $r_{\text{av}} = 5\ \text{s}^{-1}$, which equals the average feedforward rate during tuning. In Figure 3c, the attractor landscapes are approximated by computing the distance traveled by an output population bump in the untuned condition, after a cue bump has been presented for 1 s. The cue bump is a von Mises function is phase space:

$$\mathcal{B}\left(\vec{\varphi}\right) := \mathcal{B}_{\max}\exp\left(\frac{\sum_{n=0}^{2}\cos\left(\vec{\varphi}\cdot\vec{k}_n\right) - 3}{\sigma_{\mathcal{B}}^2}\right) \quad \text{with} \quad \vec{k}_n := \begin{bmatrix}\cos(n\pi/3)\\ \sin(n\pi/3)\end{bmatrix} \tag{11}$$

where $\sigma_{\mathcal{B}} = 0.1$ sets the bump width and the scaling factor $\mathcal{B}_{\max} \approx 25.8\,\text{s}^{-1}$ is chosen such that the mean feed-forward input is r_{av}. The cue bump is presented in all possible phases ($N_{\text{E}} = 900$) and the distance traveled by the output bump is recorded 15 s after cue removal.

4.3 | Model of synaptic plasticity

The recurrent excitatory weights w_{ij}^{EE} are plastic according to the Hebbian rule:

$$\frac{\text{d}w_{ij}^{\text{EE}}}{\text{d}t} := \eta\left(r_i^{\text{E}} - r_{\text{av}}\right)\left(r_j^{\text{E}} - r_{\text{av}}\right) \quad \text{with} \quad 0 \le w_{ij}^{\text{EE}} \le w_{\max} \tag{12}$$

where $\eta \ll 1$ is a small learning rate, $r_i^{\text{E}} \ge 0$ is the firing rate of excitatory neuron i, and $r_{\text{av}} > 0$ is the average input firing rate in the environment. Additionally, at each time step, the weights are additively normalized to ensure that the total input and output weight of each neuron is kept constant during learning, that is,

$$\sum_{j=1}^{N_{\text{E}}} w_{ij}^{\text{EE}} = \sum_{i=1}^{N_{\text{E}}} w_{ij}^{\text{EE}} = w_{\text{EE}}^{\text{tot}}. \tag{13}$$

At the initial condition, a random subset of $f_{EE}N_E < N_E$ excitatory weights are set to the upper bound $w_{max} = w_{EE}^{tot}/(f_{EE}N_E)$. During learning, the synaptic weights are updated every 30 ms while a virtual rat explores a square enclosure for 1,000 s. The weight constraints $0 \le w_{ij}^{EE} \le w_{max}$ are enforced at each time step of the simulation. To avoid positive feedback loops between neural and weights' dynamics, we silence the recurrent input whenever synaptic plasticity is active.

4.4 | Model of spatial exploration

The virtual rat explores a square enclosure of side-length L with an isotropic random walk at constant speed v. Virtual-rat trajectories $\mathbf{x}_t$ are sampled from the stochastic process

$$\frac{d\mathbf{X}_t}{dt} := v[\cos(\theta_t), \sin(\theta_t)] \quad \text{with} \quad \theta_t = \sigma_\theta \mathcal{W}_t, \tag{14}$$

where the angle θ_t sets the direction of motion and $\mathcal{W}_t$ is a standard Wiener process. The parameter σ_θ controls the tortuosity of the trajectory. At the boundaries of the environment, the component of the movement direction perpendicular to the boundary is inverted. Spatial locations in the arena are discretized in 100^2 square bins. The random walk is updated every 30 ms of the simulation.

4.5 | Grid-tuning index

The grid-tuning index measures the strength of triangular periodicity of a 2-dimensional (2D) signal. The index is bounded between 0 and 1. It reaches 0 when the signal is completely aperiodic and it reaches 1 when the signal is composed of infinitely small bumps of activity that lie on a periodic triangular lattice with 60° symmetry.

To compute the grid-tuning index, we first compute the 2D autocorrelation of the input firing-rate map $r(\vec{x})$. We then estimate the grid spacing T_{est} as the mean distance of the six autocorrelation peaks closest to the origin, and the grid orientation as the angle to the horizontal axis of the autocorrelation peak in the first quadrant. Next, we scale and rotate the input pattern $r(\vec{x})$ to obtain a normalized pattern $r_{norm}(\vec{x})$ that has a standard orientation of 0° and a grid spacing of L/n where n is the closest integer to L/T_{est}, i.e., we rescale the pattern such that it fits an integer number of times n in the arena. Note that in the limit of $n = 1$, we abort the procedure and we set the grid-tuning index to 0.

The grid-tuning index is obtained from the 2-dimensional Fourier series of the normalized pattern $r_{norm}(\vec{x})$ computed on a triangular lattice with 60° symmetry. Formally, we define the 2-dimensional Fourier series of a function $f(\vec{x})$ on a lattice $\mathcal{L}$ as:

$$\hat{f}(a,b) := \int_C d\vec{x} f(\vec{x}) \exp\left[-j\left(a\vec{u}_1^* \cdot \vec{x} + b\vec{u}_2^* \cdot \vec{x}\right)\right] \tag{15}$$

and

$$f(\vec{x}) = \frac{1}{V_C} \sum_{a=-\infty}^{\infty} \sum_{b=-\infty}^{\infty} \hat{f}(a,b) \exp\left[j\left(a\vec{u}_1^* \cdot \vec{x} + b\vec{u}_2^* \cdot \vec{x}\right)\right] \tag{16}$$

where $j = \sqrt{-1}$ is the imaginary unit, a, b $\in \mathbb{Z}$, $\hat{f}(a,b) \in \mathbb{C}$, and C is a primary cell with area V_C of the lattice $\mathcal{L}$ with unit vectors $\vec{u}_1, \vec{u}_2$. The vectors $\vec{u}_1^*$, $\vec{u}_2^*$ are the unit vectors of the reciprocal lattice:

$$\left[\vec{u}_1^*, \vec{u}_2^*\right] := 2\pi \left[\vec{u}_1, \vec{u}_2\right]^{-\top} \tag{17}$$

where $A^{-\top}$ is the transpose of the inverse of A. To compute the grid-tuning index, we take the Fourier series of the normalized pattern $r_{norm}(\vec{x})$ on a lattice with unit vectors of length L:

$$\vec{u}_1 := L\begin{bmatrix}\cos(\pi/6)\\ \sin(\pi/6)\end{bmatrix} = L\begin{bmatrix}\sqrt{3}/2\\ 1/2\end{bmatrix} \quad \text{and} \quad \vec{u}_2 := L\begin{bmatrix}\cos(\pi/2)\\ \sin(\pi/2)\end{bmatrix} = L\begin{bmatrix}0\\ 1\end{bmatrix}, \tag{18}$$

which yields

$$\vec{u}_1^* = \frac{4\pi}{L\sqrt{3}}\begin{bmatrix}1\\ 0\end{bmatrix}, \quad \vec{u}_2^* = \frac{4\pi}{L\sqrt{3}}\begin{bmatrix}-1/2\\ \sqrt{3}/2\end{bmatrix}, \quad \text{and} \quad V_C := \det\left[\vec{u}_1, \vec{u}_2\right] = L^2\sqrt{3}/2. \tag{19}$$

We define the grid-tuning index $\mathcal{G}$ as the average Fourier amplitude at the nth harmonic $\mathcal{K}_n := \{(n, 0), (0, n), (n, n)\}$ normalized by the total firingrate $\hat{r}_{norm}(0,0)$:

$$\mathcal{G} := \frac{1}{3\hat{r}_{norm}(0,0)} \sum_{(a,b)\in\mathcal{K}_n} |\hat{r}_{norm}(a,b)|. \tag{20}$$

In the following paragraphs, we compare the grid-tuning index $\mathcal{G}$ to a gridness score commonly adopted in the literature (Langston et al., 2010). The gridness score is computed from the 2D-autocorrelation of the firing-rate map $r(\vec{x})$ cropped within rings centered in the origin with inner radius R^{in} and outer radii $\{R_i^{out}\}$. The inner radius R^{in} is the smallest distance at which the radial profile of the autocorrelation becomes negative; the outer radii $\{R_i^{out}\}$ are increased within a set range (see below). From the ith autocorrelation ring, we compute $g_i := min[\rho_i(60) + \rho_i(120)] - max[\rho_i(30) + \rho_i(90) + \rho_i(150)]$ where $\rho_i(\varphi)$ is the Pearson's correlation coefficient between the original ring and the ring rotated by φ degrees. The gridness score is the maximal g_i that is obtained across rings of different outer radii. Langston et al. (2010) vary the outer radius from a minimum of $R^{in} + 10$ cm to a maximum of $L - 10$ cm where L is the width of the arena. However, because the fixed 10 cm offset does not generalize well across scales, we vary the outer radius between $0.5\,T_{est}$ and $2\,T_{est}$ where T_{est} is the estimated grid spacing, that is, the mean distance of the six autocorrelation peaks closest to the origin.

In Figure 8a, we compare the grid-tuning index and the gridness score for the simulations in Figure 1. We find that the two measures are positively correlated for the feedforward inputs (Spearman's rank correlation $R = 0.54$, $p < 10^{-4}$), excitatory outputs ($R = 0.52$, $p < 10^{-4}$),

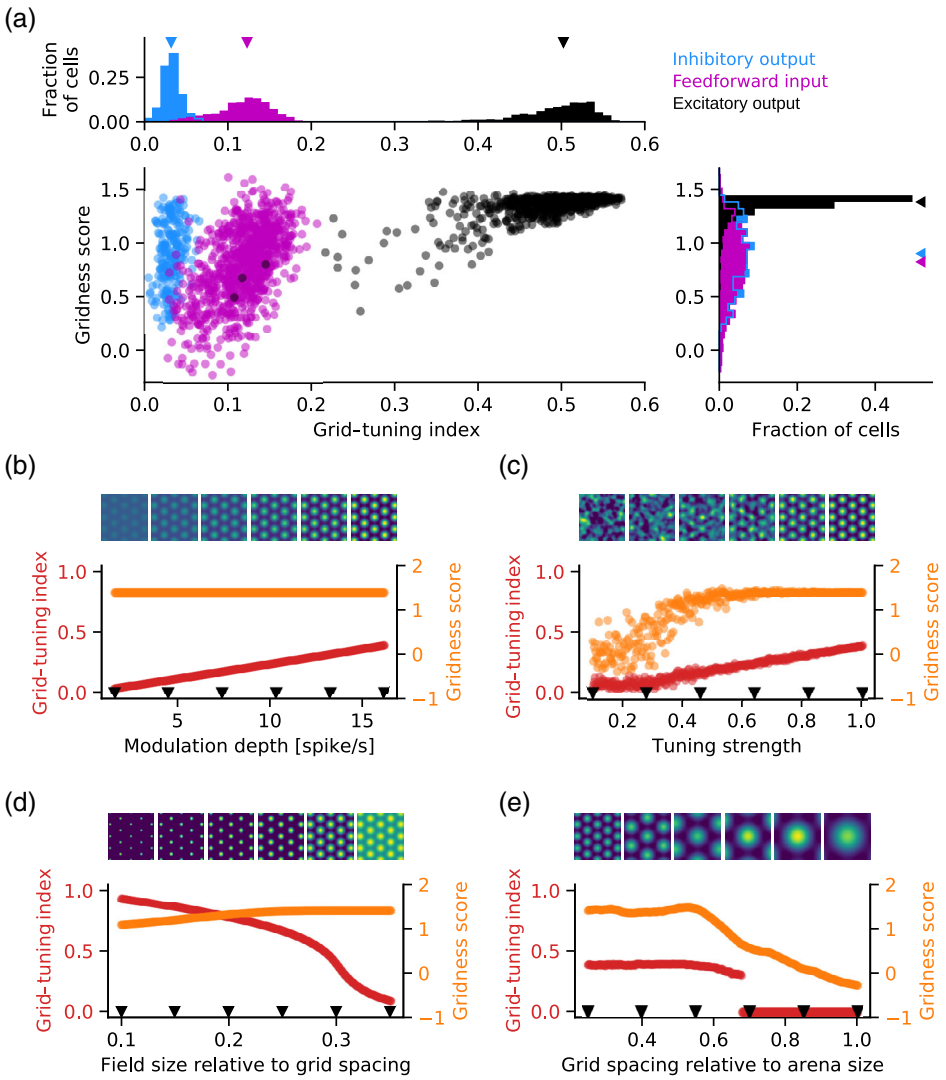

FIGURE 8 Comparison between the grid-tuning index and the gridness score. (a) Bottom-left: grid-tuning indexes and gridness scores of the feedforward inputs (magenta), excitatory outputs (black), and inhibitory outputs (blue) for the results in Figure 1. Distributions of grid-tuning indexes and gridness scores are shown at the top and right panels, respectively. Triangles indicate median values. (b–e) Bottom: grid-tuning indexes (red) and gridness scores (orange) of 400 grids with different modulation depth (b), input-tuning strength (c), grid-field size (d), and grid spacing (e). Top: six example grids with parameter values indicated by the black triangular markers in the bottom panels. Grids are generated as described in Section 4.2. Patterns in (b)–(e) have common spacing and orientation. Patterns in (b), (d), (e) have input-tuning strength $\beta = 1$. The modulation depth is the difference between the maximal and minimal firing rate in the arena [Color figure can be viewed at wileyonlinelibrary.com]

and inhibitory outputs ($R = 0.25$, $p < 10^{-3}$). However, the gridness-score distributions are broader and show larger overlaps compared to the corresponding grid-tuning-index distributions (Figure 8a, compare top and right panels).

We also note that for the inhibitory outputs gridness scores are large but grid-tuning indexes are small (Figure 8a). This difference arises from the inhibitory outputs often showing triangular periodicity with low modulation depths, that is, with small differences between maximal and minimal firing rates in the arena (see example firing-rate maps in Figure 1c2). In fact, the grid-tuning index increases linearly as a function of modulation depth, but the gridness score remains constant (Figure 8b).

Next, we compare grid-tuning index and gridness score across different input-tuning strengths, that is, the relative strength of the grid signal compared to the noise (see also Section 4.2 and Figure 5). As expected, both measures positively correlate with the input-tuning strength (Figure 8c). However, the gridness score (but not the grid-tuning index) saturates at its maximum already for intermediate input-tuning strengths, for example, for strengths larger than 0.5.

The two measures also display different trends as a function of the size of the grid fields: for larger grid fields, the grid-tuning index decreases, but the gridness score increases (Figure 8d). Finally, for grid spacings that are large compared to the size of the environment (Figure 8e), both measures decay. Yet they do so in a different manner: the gridness score decreases smoothly, whereas the grid-tuning index jumps to 0 whenever the spectrum of the spatial map is dominated by the first harmonic, that is, when the closest integer to L/T_{est} equals 1.

In summary, the grid-tuning index is sensible to the modulation depth of the firing-rate pattern, increases for smaller grid fields, and has a larger dynamic range as compared to the measure proposed by (Langston et al., 2010). For these reasons, we think that our measure is better suited to quantify "gridness" than the classical score.

4.6 | Connectivity-tuning index

The connectivity-tuning index measures the strength of the first harmonic of the recurrent excitatory weights w_{ij}^{EE}. To formally define this index, we first introduce the excitatory input-weight function

$$\mathcal{W}_i\left(\vec{\varphi}_j\right) := w_{ij}^{EE} \tag{21}$$

where $\vec{\varphi}_j$ is the grid phase of presynaptic neuron j. We then compute the 2-dimensional Fourier series $\widehat{\mathcal{W}}_i(a,b)$ of $\mathcal{W}_i\left(\vec{\varphi}_j\right)$ on a lattice $\mathscr{L}$ with unit vectors (Equation (15)):

$$\vec{u}_1 := 2\pi\begin{bmatrix}\cos(\pi/6)\\ \sin(\pi/6)\end{bmatrix} = 2\pi\begin{bmatrix}\sqrt{3}/2\\ 1/2\end{bmatrix} \text{ and}$$
$$\vec{u}_2 := 2\pi\begin{bmatrix}\cos(\pi/2)\\ \sin(\pi/2)\end{bmatrix} = 2\pi\begin{bmatrix}0\\ 1\end{bmatrix}. \tag{22}$$

The connectivity-tuning index $\mathcal{C}$ is computed by averaging across all postsynaptic neurons i the amplitude of the first harmonic of $\mathcal{W}_i$ normalized by the total input weight $\widehat{\mathcal{W}}_i(0,0)$:

$$\mathcal{C} := \frac{1}{N_E}\sum_{i=1}^{N_E}\frac{1}{3\widehat{\mathcal{W}}_i(0,0)}\sum_{(a,b)\in\mathscr{K}_1}\left|\widehat{\mathcal{W}}_i(a,b)\right| \tag{23}$$

where $\mathscr{K}_1 := \{(1,0),(0,1),(1,1)\}$ is the first harmonic.

ACKNOWLEDGMENTS

We thank Eric Reifenstein and Paul Pfeiffer for stimulating discussions and feedback on the manuscript. This work is funded by the German Federal Ministry of Education and Research (BMBF, grant 01GQ1705) and by the Deutsche Forschungsgemeinschaft (DFG, German Research Foundation; project numbers 327654276—SFB 1315 and KE788/3-1—SPP 1665). Open access funding enabled and organized by Projekt DEAL.

CONFLICT OF INTEREST

The authors declare that they have no conflict of interest.

DATA AVAILABILITY STATEMENT

Data sharing is not applicable to this article as no new data were created or analyzed in this study. The source code of all numerical simulations is available at http://modeldb.yale.edu/262356.

ORCID

Tiziano D'Albis https://orcid.org/0000-0003-1585-1433
Richard Kempter https://orcid.org/0000-0002-5344-2983

REFERENCES

Alonso, A., De Curtis, M., & Llinas, R. (1990). Postsynaptic Hebbian and non-Hebbian long-term potentiation of synaptic efficacy in the entorhinal cortex in slices and in the isolated adult Guinea pig brain. *Proceedings of the National Academy of Sciences of the United States of America*, *87*, 9280–9284.

Barry, C., Ginzberg, L. L., O'Keefe, J., & Burgess, N. (2012). Grid cell firing patterns signal environmental novelty by expansion. *Proceedings of the National Academy of Sciences of the United States of America*, *109*, 17687–17692.

Barry, C., Hayman, R., Burgess, N., & Jeffery, K. J. (2007). Experience-dependent rescaling of entorhinal grids. *Nature Neuroscience*, *10*, 682–684.

Beed, P., Gundlfinger, A., Schneiderbauer, S., Song, J., Böhm, C., Burgalossi, A., … Schmitz, D. (2013). Inhibitory gradient along the dorsoventral axis in the medial entorhinal cortex. *Neuron*, *79*, 1197–1207.

Ben-Yishai, R., Bar-Or, R. L., & Sompolinsky, H. (1995). Theory of orientation tuning in visual cortex. *Proceedings of the National Academy of Sciences of the United States of America*, *92*, 3844–3848.

Boccara, C. N., Sargolini, F., Thoresen, V. H., Solstad, T., Witter, M. P., Moser, E. I., & Moser, M.-B. (2010). Grid cells in pre-and parasubiculum. *Nature Neuroscience*, *13*, 987–994.

Buetfering, C., Allen, K., & Monyer, H. (2014). Parvalbumin interneurons provide grid cell-driven recurrent inhibition in the medial entorhinal cortex. *Nature Neuroscience*, *17*, 710–718.

Burak, Y., & Fiete, I. R. (2009). Accurate path integration in continuous attractor network models of grid cells. *PLoS Computational Biology*, *5*, 1–16.

Carandini, M., & Ringach, D. L. (1997). Predictions of a recurrent model of orientation selectivity. *Vision Research*, *37*, 3061–3071.

Castro, L., & Aguiar, P. (2014). A feedforward model for the formation of a grid field where spatial information is provided solely from place cells. *Biological Cybernetics*, *108*, 133–143.

Chen, G., Manson, D., Cacucci, F., & Wills, T. J. (2016). Absence of visual input results in the disruption of grid cell firing in the mouse. *Current Biology*, *26*, 2335–2342.

Couey, J. J., Witoelar, A., Zhang, S.-J., Zheng, K., Ye, J., Dunn, B., … Witter, M. P. (2013). Recurrent inhibitory circuitry as a mechanism for grid formation. *Nature Neuroscience*, *16*, 318–324.

D'Albis, T., & Kempter, R. (2017). A single-cell spiking model for the origin of grid-cell patterns. *PLoS Computational Biology*, *13*, e1005782.

de Curtis, M., & Llinas, R. R. (1993). Entorhinal cortex long-term potentiation evoked by theta-patterned stimulation of associative fibers in the isolated in vitro Guinea pig brain. *Brain Research*, *600*, 327–330.

Deng, P.-Y., & Lei, S. (2007). Long-term depression in identified stellate neurons of juvenile rat entorhinal cortex. *Journal of Neurophysiology*, *97*, 727–737.

Dhillon, A., & Jones, R. S. (2000). Laminar differences in recurrent excitatory transmission in the rat entorhinal cortex in vitro. *Neuroscience*, *99*, 413–422.

Diehl, G. W., Hon, O. J., Leutgeb, S., & Leutgeb, J. K. (2017). Grid and nongrid cells in medial entorhinal cortex represent spatial location and environmental features with complementary coding schemes. *Neuron*, *94*, 83–92.

Dordek, Y., Soudry, D., Meir, R., & Derdikman, D. (2016). Extracting grid cell characteristics from place cell inputs using non-negative principal component analysis. *eLife*, *5*, e10094.

Douglas, R. J., Koch, C., Mahowald, M., Martin, K., & Suarez, H. H. (1995). Recurrent excitation in neocortical circuits. *Science*, *269*, 981–985.

Dunn, B., Mørreaunet, M., & Roudi, Y. (2015). Correlations and functional connections in a population of grid cells. *PLoS Computational Biology*, *11*, e1004052.

Etienne, A. S., & Jeffery, K. J. (2004). Path integration in mammals. *Hippocampus*, *14*, 180–192.

Fuchs, E. C., Neitz, A., Pinna, R., Melzer, S., Caputi, A., & Monyer, H. (2016). Local and distant input controlling excitation in layer II of the medial entorhinal cortex. *Neuron*, *89*, 194–208.

Fuhs, M. C., & Touretzky, D. S. (2006). A spin glass model of path integration in rat medial entorhinal cortex. *The Journal of Neuroscience*, *26*, 4266–4276.

Fujimaru, Y., & Kosaka, T. (1996). The distribution of two calcium binding proteins, calbindin D-28K and parvalbumin, in the entorhinal cortex of the adult mouse. *Neuroscience Research*, *24*, 329–343.

Gardner, R. J., Lu, L., Wernle, T., Moser, M.-B., & Moser, E. I. (2019). Correlation structure of grid cells is preserved during sleep. *Nature Neuroscience*, *22*, 598–608.

Gil, M., Ancau, M., Schlesiger, M. I., Neitz, A., Allen, K., De Marco, R. J., & Monyer, H. (2018). Impaired path integration in mice with disrupted grid cell firing. *Nature Neuroscience*, *21*, 81–91.

Gu, Y., Lewallen, S., Kinkhabwala, A. A., Domnisoru, C., Yoon, K., Gauthier, J. L., … Tank, D. W. (2018). A map-like micro-organization of grid cells in the medial entorhinal cortex. *Cell*, *175*, 736–750.

Guanella, A., Kiper, D., & Verschure, P. (2007). A model of grid cells based on a twisted torus topology. *International Journal of Neural Systems*, *17*, 231–240.

Hafting, T., Fyhn, M., Bonnevie, T., Moser, M.-B., & Moser, E. I. (2008). Hippocampus-independent phase precession in entorhinal grid cells. *Nature*, *453*, 1248–1252.

Hafting, T., Fyhn, M., Molden, S., Moser, M.-B., & Moser, E. I. (2005). Microstructure of a spatial map in the entorhinal cortex. *Nature*, *436*, 801–806.

Hahnloser, R. (2003). Emergence of neural integration in the head-direction system by visual supervision. *Neuroscience*, *120*, 877–891.

Hardcastle, K., Ganguli, S., & Giocomo, L. M. (2015). Environmental boundaries as an error correction mechanism for grid cells. *Neuron*, *86*, 827–839.

Hasselmo, M. E. (2006). The role of acetylcholine in learning and memory. *Current Opinion in Neurobiology*, *16*, 710–715.

Heys, J. G., Rangarajan, K. V., & Dombeck, D. A. (2014). The functional micro-organization of grid cells revealed by cellular-resolution imaging. *Neuron*, *84*, 1079–1090.

Holmgren, C., Harkany, T., Svennenfors, B., & Zilberter, Y. (2003). Pyramidal cell communication within local networks in layer 2/3 of rat neocortex. *The Journal of Physiology*, *551*, 139–153.

Itskov, V., Hansel, D., & Tsodyks, M. (2011). Short-term facilitation may stabilize parametric working memory trace. *Frontiers in Computational Neuroscience*, *5*, 40.

Kang, L., & Balasubramanian, V. (2019). A geometric attractor mechanism for self-organization of entorhinal grid modules. *eLife*, *8*, e46687.

Kilpatrick, Z. P., Ermentrout, B., & Doiron, B. (2013). Optimizing working memory with heterogeneity of recurrent cortical excitation. *The Journal of Neuroscience*, *33*, 18999–19011.

Kitamura, T., Pignatelli, M., Suh, J., Kohara, K., Yoshiki, A., Abe, K., & Tonegawa, S. (2014). Island cells control temporal association memory. *Science*, *343*, 896–901.

Ko, H., Cossell, L., Baragli, C., Antolik, J., Clopath, C., Hofer, S. B., & Mrsic-Flogel, T. D. (2013). The emergence of functional microcircuits in visual cortex. *Nature*, *496*, 96–100.

Kohn, A., & Smith, M. A. (2005). Stimulus dependence of neuronal correlation in primary visual cortex of the macaque. *The Journal of Neuroscience*, *25*, 3661–3673.

Kropff, E., Carmichael, J. E., Moser, M.-B., & Moser, E. I. (2015). Speed cells in the medial entorhinal cortex. *Nature*, *523*, 419–424.

Kropff, E., & Treves, A. (2008). The emergence of grid cells: Intelligent design or just adaptation? *Hippocampus*, *18*, 1256–1269.

Krupic, J., Bauza, M., Burton, S., & O'Keefe, J. (2016). Framing the grid: Effect of boundaries on grid cells and navigation. *The Journal of Physiology*, *594*, 6489–6499.

Lampl, I., Reichova, I., & Ferster, D. (1999). Synchronous membrane potential fluctuations in neurons of the cat visual cortex. *Neuron*, *22*, 361–374.

Langston, R. F., Ainge, J. A., Couey, J. J., Canto, C. B., Bjerknes, T. L., Witter, M. P., … Moser, M.-B. (2010). Development of the spatial representation system in the rat. *Science*, *328*, 1576–1580.

Lien, A. D., & Scanziani, M. (2013). Tuned thalamic excitation is amplified by visual cortical circuits. *Nature Neuroscience*, *16*, 1315–1323.

Mathis, A., Herz, A. V., & Stemmler, M. (2012). Optimal population codes for space: Grid cells outperform place cells. *Neural Computation*, *24*, 2280–2317.

McNaughton, B. L., Battaglia, F. P., Jensen, O., Moser, E. I., & Moser, M.-B. (2006). Path integration and the neural basis of the 'cognitive map'. *Nature Reviews. Neuroscience*, *7*, 663–678.

Mhatre, H., Gorchetchnikov, A., & Grossberg, S. (2012). Grid cell hexagonal patterns formed by fast self-organized learning within entorhinal cortex. *Hippocampus*, *22*, 320–334.

Miao, C., Cao, Q., Moser, M.-B., & Moser, E. I. (2017). Parvalbumin and somatostatin interneurons control different space-coding networks in the medial entorhinal cortex. *Cell*, *171*, 507–521.

Monsalve-Mercado, M. M., & Leibold, C. (2017). Hippocampal spike-timing correlations lead to hexagonal grid fields. *Physical Review Letters*, *119*, 038101.

Murphy, B. K., & Miller, K. D. (2009). Balanced amplification: A new mechanism of selective amplification of neural activity patterns. *Neuron*, *61*, 635–648.

Naumann, R., Preston-Ferrer, P., Brecht, M., & Burgalossi, A. (2018). Structural modularity and grid activity in the medial entorhinal cortex. *Journal of Neurophysiology*, *119*, 2129–2144.

Naumann, R. K., Ray, S., Prokop, S., Las, L., Heppner, F. L., & Brecht, M. (2016). Conserved size and periodicity of pyramidal patches in layer 2 of medial/caudal entorhinal cortex. *The Journal of Comparative Neurology*, *524*, 783–806.

Navratilova, Z., Giocomo, L. M., Fellous, J.-M., Hasselmo, M. E., & McNaughton, B. L. (2012). Phase precession and variable spatial scaling in a periodic attractor map model of medial entorhinal grid cells with realistic after-spike dynamics. *Hippocampus*, *22*, 772–789.

Ocko, S. A., Hardcastle, K., Giocomo, L. M., & Ganguli, S. (2018). Emergent elasticity in the neural code for space. *Proceedings of the National Academy of Sciences of the United States of America*, *115*, E11798–E11806.

Ólafsdóttir, H. F., Carpenter, F., & Barry, C. (2016). Coordinated grid and place cell replay during rest. *Nature Neuroscience*, *19*, 792–794.

Pastoll, H., Solanka, L., van Rossum, M. C., & Nolan, M. F. (2013). Feedback inhibition enables theta-nested gamma oscillations and grid firing fields. *Neuron*, *77*, 141–154.

Pérez-Escobar, J. A., Kornienko, O., Latuske, P., Kohler, L., & Allen, K. (2016). Visual landmarks sharpen grid cell metric and confer context specificity to neurons of the medial entorhinal cortex. *eLife*, *5*, e16937.

Perin, R., Berger, T. K., & Markram, H. (2011). A synaptic organizing principle for cortical neuronal groups. *Proceedings of the National Academy of Sciences of the United States of America*, *108*, 5419–5424.

Ray, S., Naumann, R., Burgalossi, A., Tang, Q., Schmidt, H., & Brecht, M. (2014). Grid-layout and theta-modulation of layer 2 pyramidal neurons in medial entorhinal cortex. *Science*, *343*, 891–896.

Rowland, D. C., Roudi, Y., Moser, M.-B., & Moser, E. I. (2016). Ten years of grid cells. *Annual Review of Neuroscience*, *39*, 19–40.

Sargolini, F., Fyhn, M., Hafting, T., McNaughton, B. L., Witter, M. P., Moser, M.-B., & Moser, E. I. (2006). Conjunctive representation of position, direction, and velocity in entorhinal cortex. *Science*, *312*, 758–762.

Savelli, F., Yoganarasimha, D., & Knierim, J. J. (2008). Influence of boundary removal on the spatial representations of the medial entorhinal cortex. *Hippocampus*, *18*, 1270–1282.

Schmidt, H., Gour, A., Straehle, J., Boergens, K. M., Brecht, M., & Helmstaedter, M. (2017). Axonal synapse sorting in medial entorhinal cortex. *Nature*, *549*, 469–475.

Si, B., Kropff, E., & Treves, A. (2012). Grid alignment in entorhinal cortex. *Biological Cybernetics*, *106*, 483–506.

Si, B., & Treves, A. (2013). A model for the differentiation between grid and conjunctive units in medial entorhinal cortex. *Hippocampus*, *23*, 1410–1424.

Solger, J., Wozny, C., Manahan-Vaughan, D., & Behr, J. (2004). Distinct mechanisms of bidirectional activity-dependent synaptic plasticity in superficial and deep layers of rat entorhinal cortex. *The European Journal of Neuroscience*, *19*, 2003–2007.

Somers, D. C., Nelson, S. B., & Sur, M. (1995). An emergent model of orientation selectivity in cat visual cortical simple cells. *The Journal of Neuroscience*, *15*, 5448–5465.

Stensola, H., Stensola, T., Solstad, T., Frøland, K., Moser, M.-B., & Moser, E. I. (2012). The entorhinal grid map is discretized. *Nature*, *492*, 72–78.

Stepanyants, A., & Chklovskii, D. B. (2005). Neurogeometry and potential synaptic connectivity. *Trends in Neurosciences*, *28*, 387–394.
Stepanyuk, A. (2015). Self-organization of grid fields under supervision of place cells in a neuron model with associative plasticity. *Biologically Inspired Cognitive Architectures*, *13*, 48–62.
Stringer, S., Trappenberg, T., Rolls, E., & De Araujo, I. (2002). Self-organizing continuous attractor networks and path integration: One-dimensional models of head direction cells. *Network: Computation in Neural Systems*, *13*, 217–242.
Suarez, H., Koch, C., & Douglas, R. (1995). Modeling direction selectivity of simple cells in striate visual cortex within the framework of the canonical microcircuit. *The Journal of Neuroscience*, *15*, 6700–6719.
Tennant, S. A., Fischer, L., Garden, D. L., Gerlei, K. Z., Martinez-Gonzalez, C., McClure, C., … Nolan, M. F. (2018). Stellate cells in the medial entorhinal cortex are rired for spatial learning. *Cell Reports*, *22*, 1313–1324.
Tocker, G., Barak, O., & Derdikman, D. (2015). Grid cells correlation structure suggests organized feedforward projections into superficial layers of the medial entorhinal cortex. *Hippocampus*, *25*, 1599–1613.
Trettel, S. G., Trimper, J. B., Hwaun, E., Fiete, I. R., & Colgin, L. L. (2019). Grid cell co-activity patterns during sleep reflect spatial overlap of grid fields during active behaviors. *Nature Neuroscience*, *22*, 609–617.
Urdapilleta, E., Si, B., & Treves, A. (2017). Self-organization of modular activity of grid cells. *Hippocampus*, *27*, 1204–1213.
Weber, S. N., & Sprekeler, H. (2018). Learning place cells, grid cells and invariances with excitatory and inhibitory plasticity. *eLife*, *7*, e34560.
Welinder, P. E., Burak, Y., & Fiete, I. R. (2008). Grid cells: The position code, neural network models of activity, and the problem of learning. *Hippocampus*, *18*, 1283–1300.
Widloski, J., & Fiete, I. R. (2014). A model of grid cell development through spatial exploration and spike time-dependent plasticity. *Neuron*, *83*, 481–495.
Wills, T. J., Cacucci, F., Burgess, N., & O'Keefe, J. (2010). Development of the hippocampal cognitive map in preweanling rats. *Science*, *328*, 1573–1576.
Winterer, J., Maier, N., Wozny, C., Beed, P., Breustedt, J., Evangelista, R., … Schmitz, D. (2017). Excitatory microcircuits within superficial layers of the medial entorhinal cortex. *Cell Reports*, *19*, 1110–1116.
Yang, S., Lee, D., Chung, C., Cheong, M., Lee, C.-J., & Jung, M. (2004). Long-term synaptic plasticity in deep layer-originated associational projections to superficial layers of rat entorhinal cortex. *Neuroscience*, *127*, 805–812.
Yoon, K., Buice, M. A., Barry, C., Hayman, R., Burgess, N., & Fiete, I. R. (2013). Specific evidence of low-dimensional continuous attractor dynamics in grid cells. *Nature Neuroscience*, *16*, 1077–1084.
Yun, S. H., Mook-Jung, I., & Jung, M. W. (2002). Variation in effective stimulus patterns for induction of long-term potentiation across different layers of rat entorhinal cortex. *The Journal of Neuroscience*, *22*, RC214.
Zhang, K. (1996). Representation of spatial orientation by the intrinsic dynamics of the head-direction cell ensemble: A theory. *The Journal of Neuroscience*, *16*, 2112–2126.
Zhong, W., Lu, Z., Schwab, D. J., & Murugan, A. (2020). Nonilibrium statistical mechanics of continuous attractors. *Neural Computation*, *32*, 1033–1068.
Zhou, Y.-D., Acker, C. D., Netoff, T. I., Sen, K., & White, J. A. (2005). Increasing Ca^{2+} transients by broadening postsynaptic action potentials enhances timing-dependent synaptic depression. *Proceedings of the National Academy of Sciences of the United States of America*, *102*, 19121–19125.

How to cite this article: D'Albis T, Kempter R. Recurrent amplification of grid-cell activity. *Hippocampus*. 2020;30:1268–1297. https://doi.org/10.1002/hipo.23254

APPENDIX A: One-dimensional grid-amplification model

Here, we formulate a minimal mathematical model for the recurrent amplification of grid-cell activity on linear tracks. This model captures the main features of grid-pattern amplification, is analytically tractable, and can be understood intuitively.

We model the activity of a recurrent network as a virtual rat runs at constant speed on a one-dimensional linear track. The feedforward inputs are noisy grids as a function of space. All input grids share the same spatial frequency, but have different spatial phases. Hence, each neuron in the network is identified by the spatial phase φ of its feedforward input h. We term this phase the *preferred spatial phase* of a neuron (Figure A1a,b).

Output activity

We assume that all preferred phases φ are evenly sampled in the range $[-\pi, \pi]$. Therefore, in the limit of a large number of neurons, the output activity of the network obeys

$$\tau \frac{\mathrm{d}}{\mathrm{d}t} v(\varphi, x) := -v(\varphi, x) + F\left(h(\varphi, x) + \int_{-\pi}^{\pi} \mathrm{d}\varphi' M(\varphi - \varphi')\, v(\varphi', x)\right) \quad \text{(A1)}$$

where x is the position of the virtual rat on the track, $h(\varphi, x)$ is the total feedforward input to neuron φ, the function $M(\varphi - \varphi')$ sets the connection strength from neuron φ' to neuron φ, the variable $\tau > 0$ controls the integration time constant of the network, and F is the neuronal activation function. We use a linear activation function $F(x) := x$ in Figures A2, A3, A4a, A5a, A6, and in all analytical derivations (Appendix B). We use a threshold-linear activation function $F(x) := [x]_+$ where $[x]_+ = x$ if $x > 0$, and $[x]_+ = 0$ otherwise in Figures A4b and A5b. We consider a finite number $N = 200$ of neurons in all numerical simulations. Parameter values are summarized in Table A1.

Compared to the two-dimensional (2D) network model in Section 2 (see Section 4.1 and Equations (1)–(3)), we made the following simplifications: (a) the two populations of N_E excitatory and N_I inhibitory neurons with rates r_i^E and r_i^I are replaced by a single population of infinitely many units with activity $v(\varphi, x)$; (b) the connectivity matrices $W_{ij}^{EE}, W_{ij}^{IE}, W_{ij}^{EI}$, and W_{ij}^{II} are replaced by a single connectivity function M; (c) The connectivity function M is already tuned with respect to the preferred phases of the cells, that is, synaptic plasticity and learning are not modeled here.

Recurrent connectivity

We assume that neurons with similar preferred phases are strongly excitatory connected, whereas neurons with dissimilar phases are weakly excitatory connected or inhibited:

$$M(\varphi - \varphi') := \frac{M_{\max}}{\pi} \cos(\varphi - \varphi') \quad \text{(A2)}$$

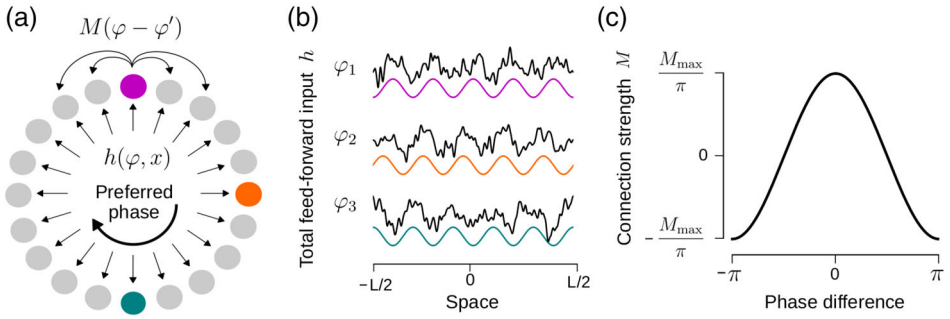

FIGURE A1 One-dimensional grid-amplification model. (a) Cartoon of the modeled neuronal network. Each neuron receives a total feedforward input $h(\varphi, x)$, which is a noisy grid in space (x) with phase φ. Neurons (disks) are arranged according to the grid phase φ of their total feedforward input (preferred phase). Colored disks indicate neurons with preferred phases $\varphi_1 = 0$ (magenta), $\varphi_2 = \pi/2$ (orange), and $\varphi_3 = \pi$ (green). The recurrent connectivity is defined by the function M, which depends only on the phase difference $\varphi - \varphi'$ between two neurons. (b) Feedforward inputs to the network. The black traces show the total feedforward input h to three example neurons with preferred phases $\varphi_1 = 0$, $\varphi_2 = \pi/2$, and $\varphi_3 = \pi$. The colored traces indicate the underlying grid-tuning function g with phases φ_1, φ_2, and φ_3 (Equation (A3), see colored disks in panel (a). (c) Recurrent-connectivity function. The parameter $M_{max} > 0$ scales the maximal connection strength in the network (Equation (A2)) [Color figure can be viewed at wileyonlinelibrary.com]

TABLE A1 Parameters of the one-dimensional grid-amplification model

Neural activity		
N	200	Number of neurons (only for numerical simulations)
L	5 m	Length of the circular track
τ	10 ms	Network integration time constant
f	1 m^{-1}	Grid spatial frequency
M_{max}	2/3	Maximal connection strength (linear model)
B	0.4	Input-tuning strength
σ_φ	$2\pi/N \approx 0.03$	Noise correlation length across neurons
σ_x	0.1	Noise correlation length in space
Derived quantities (linear model)		
A_{pop}	9	Population level amplification at the first harmonic
A_{cell}	≈7.9	Single-cell amplification at the tuning harmonic Lf
A_{noise}	≈1.2	Single-cell amplification at non-tuning harmonics

Note: The table reports the default parameter values for all numerical simulations and analytical calculations of the 1D grid-amplification model. Note that in Figures A4b and A5b, we use a nonlinear activation function $F(x) := [x]_+$ and a maximal connection strength $M_{max} = 6$.

where $M_{max} > 0$ sets the maximal connection strength in the network, and the factor $1/\pi$ is for mathematical convenience (Figure A1c). Such a connectivity resembles the one emerging via Hebbian synaptic plasticity in the 2D model of Section 2 (Figure 1). Note, however, that the connectivity function M in Equation (A2) takes both positive and negative values, that is, it models the compound effects of both excitatory and inhibitory synapses.

Input spatial tuning

The total feedforward input h to a neuron with preferred phase φ is

$$h(\varphi,x) := Bg(\varphi,x) + (1-B)\xi(\varphi,x) \quad \text{with} \quad g(\varphi,x) := \cos(2\pi fx + \varphi) \tag{A3}$$

where g is the input grid signal, ξ is the input noise, and the parameter $0 \le B \le 1$ scales the input-tuning strength. Note that the 1D input-tuning strength B in Equation (A3) corresponds to the input-tuning strength β in the 2D model (Equation (5)).

The input noise $\xi(\varphi, x)$ is a two-dimensional Gaussian random field with zero mean and autocorrelation $C_\xi(\tau_\varphi, \tau_x)$. We consider noise autocorrelation functions of the form:

$$C_\xi(\tau_\varphi,\tau_x) := \langle \xi(\varphi,x)\xi(\varphi+\tau_\varphi, x+\tau_x)\rangle_{\varphi,x} \tag{A4}$$

$$= \frac{1}{2}\mathcal{M}(\tau_\varphi;\sigma_\varphi)\mathcal{M}(2\pi\tau_x/L;\sigma_x) \tag{A5}$$

where $\mathcal{M}(\tau,\sigma) := \exp[(\cos(\tau)-1)/\sigma^2]$ is a von Mises function with spread $\sigma > 0$, and the factor 1/2 ensures that signal and noise have equal variance. The parameters σ_φ and σ_x control the noise correlation lengths across neurons and across space, respectively. See also Equations (8)–(10) for similar correlation functions in the 2D model.

For $\sigma_\varphi \to 0$, the noise is uncorrelated across neurons. For increasing values of σ_φ, larger and larger groups of neurons receive correlated activity, and correlations are stronger between neurons with nearby phases. Similarly, for $\sigma_x \to 0$, the noise is uncorrelated across spatial locations, and for larger values of σ_x it becomes increasingly smooth in space. Note that we consider only fully separable autocorrelation functions C_ξ, meaning that correlations across space and neurons are orthogonal. Also note that the input-noise variance $C_\xi(0, 0) = 1/2$ is independent of the correlation lengths σ_φ and σ_x.

Network activity at the population and single-cell levels

To quantify grid-pattern amplification, we study the network's activity at two different levels: the population level and the single-cell level. We thus introduce the following notation. We call $h(\varphi, x_0)$ the *population* feedforward input to the network for the virtual rat being at location x_0 on the track, and we call $h(\varphi_0, x)$ the *single-cell* feedforward input to a neuron with preferred phase φ_0. Consistently, we call $v(\varphi, x_0)$ the population output at location x_0, and $v(\varphi_0, x)$ the single-cell output of neuron φ_0. In what follows we study amplification at the population level (Section A.1) and at single-cell level (Section A.2).

A.1 | Amplification at the population level

In Appendix B (Section B.1), we solve the network dynamics in Equation (A1) in the linear regime, that is, with activation function $F(x) := x$. There we show that, if the recurrent connections are not too strong ($M_{\max} < 1$), the population output $v(\varphi, x_0)$ converges to a stable fixed point $v_\infty(\varphi, x_0)$ at any spatial location x_0 on the track. Importantly, at the steady-state output, the recurrent connections amplify the power of the population input at the first harmonic by a factor

$$A_{\text{pop}} \overset{(A15)}{=} \frac{1}{(1-M_{\max})^2} > 1. \tag{A6}$$

Figure A2 shows an example of this effect. Because the feedforward input is assumed to be weakly grid-tuned, a noisy activity bump is already present at the population input (Figure A2a1), and the input power is dominated by the first harmonic (Figure A2a2). At the output (Figure A2c), the first harmonic of the population input is amplified by a factor $A_{\text{pop}} = 9$ whereas all other harmonics are left unchanged (Figure A2c2). This effect is quantified by the power of the equivalent *population feedforward filter* of the network (Figure A2b), that is, the ratio of the population output and input power spectra at steady state (Section B.1). Note that, at the population level, the amplification factor A_{pop} depends only on the maximal connection strength $M_{\max}$, that is, it is independent of the parameters B, σ_φ, and σ_x that control the input spatial tuning. See also Figure 6a for an example of population-level amplification in the 2D model.

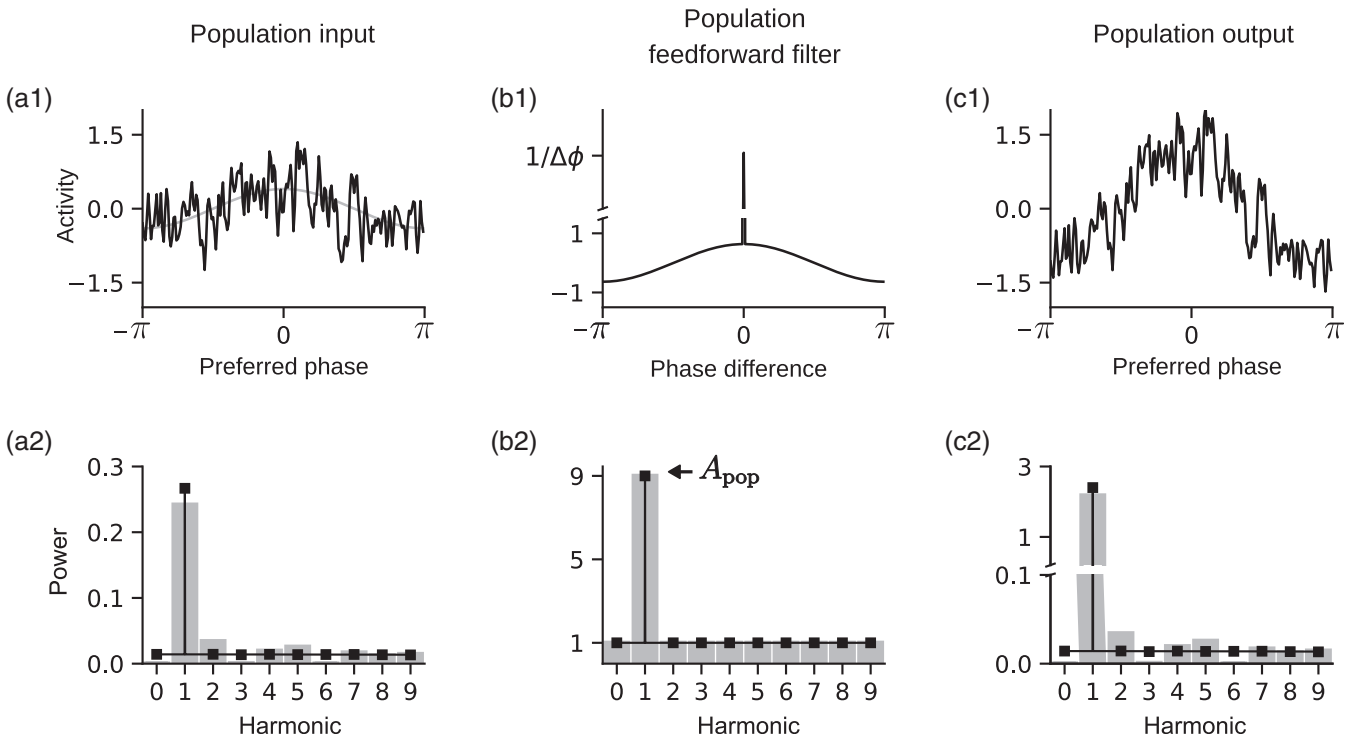

FIGURE A2 Amplification at the population level. (a) Population feedforward input $h(\varphi, x_0)$ to the network for the virtual rat being at location $x_0 = 0$ on the track. (a1) Example of the population input $h(\varphi, x_0)$ (black line) for a single realization of the input noise. Note a noisy bump of activity centered at preferred phase $\varphi = 0$. The gray line indicates the underlying input tuning. (a2) Gray bars: power spectrum of the signal in (a1) (the first 10 harmonics are shown). Black squares: average power spectrum estimated from 80 realizations of the input noise. Black line: analytical power spectrum (Section B.1, Equations (A26), (A27), and (A29)). (b) Equivalent population feedforward filter of the network (b1) and its power spectrum (b2). The black lines in (b1) and (b2) show the analytical solutions in Equations (A16) and (A15), respectively. Gray bars in (c2) are obtained by dividing the power spectrum in (c2) (gray bars) by the power spectrum in (a2) (gray bars). Black squares in (b2) are obtained by dividing the average power spectrum in (c2) (black squares) by the average power spectrum in (a2) (black squares). (c) Population steady-state output $v_\infty(\varphi, x_0)$ of the network (c1) and its power spectrum (c2). The analytical power spectrum in (c2) (black line) is derived in Section B.1 (Equation (A32)). Note that the first harmonic of the population input is amplified by a factor $A_{\text{pop}} = 9$ at the steady-state output. See Table A1 for parameter values

A.2 | Amplification at the single-cell level

We now illustrate that the recurrent dynamics also improves the grid tuning at the single-cell level (Figure A3). Because the feedforward input is assumed to be weakly grid-tuned with spatial frequency $f = 1\ \mathrm{m}^{-1}$ on a track of length $L = 5$ m (Figure A3a1), the input power spectrum is dominated by the tuning harmonic $Lf = 5$ (Figure A3a2). Crucially, this harmonic is also amplified at the steady-state output (Figure A3c). Single-cell amplification is quantified by the power of the equivalent *single-cell feedforward filter* of the network, that is, the ratio of the single-cell output and input power spectra at steady state (Figure A3b2). In the example of Figure A3, the feedforward input is amplified by a factor $A_{\mathrm{cell}} \approx 7.9$ at the tuning harmonic and by a lower factor $A_{\mathrm{noise}} \approx 1.2$ at all other frequencies (Equation (A70)). See also Figure 1 for an example of single-cell grid-pattern amplification in the 2D model.

A.2.1 | Effects of input tuning on grid pattern amplification

We now study how amplification at the single-cell level depends on the tuning of the feedforward inputs (see also Section 2.3 and Figure 4 for the corresponding results in the 2D model). To this end, we vary the input-tuning strength B (Equation (A3)) between 0 (pure noise) and 1 (pure grid), and we compute the one-dimensional (1D) grid-tuning index at both the feedforward input and steady-state output. We define the 1D grid-tuning index as the power of the neural activity at the tuning harmonic ($Lf = 5$) normalized by the power at the zeroth harmonic (see also Section 4.5 for an analogous definition of the grid-tuning index in the 2D model). Figure A4a1 shows the 1D grid-tuning index as a function of the input-tuning strength B. The 1D grid-tuning index is larger at the steady-state output compared to the feedforward input for all values of $B > 0$, consistently with the results obtained in 2D.

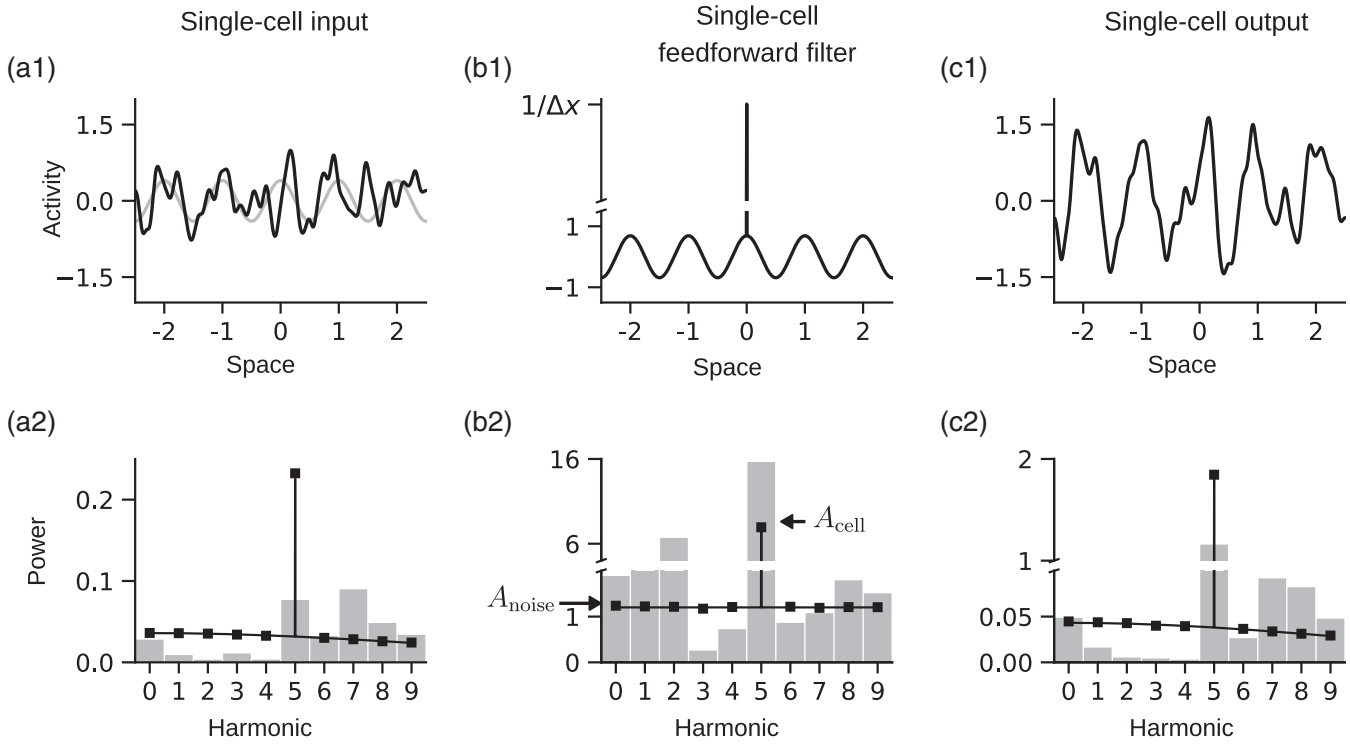

FIGURE A3 Amplification at the single-cell level. (a) Single-cell feedforward input $h(\varphi, x_0)$ to a cell with preferred phase $\varphi_0 = 0$. (a1) Single-cell input $h(\varphi, x_0)$ (black line) for one example realization of the input noise. The gray line indicates the underlying input tuning. (a2) Gray bars: power spectrum of the trace in (a1) (the first 10 harmonics are shown). Black squares: average power spectrum estimated from 80 realizations of the input noise. Black line: analytical power spectrum (Section B.2, Equations (A38), (A39), and (A42)). (b) Equivalent single-cell feedforward filter of the network (b1) and its power spectrum (b2). The black lines in (b1) and (b2) depict the analytical solutions in Equations (A73) and (A70), respectively. Gray bars in (b2) are obtained by dividing the power spectrum in (c2) (gray bars) by the power spectrum in (a2) (gray bars). Black squares in (b2) are obtained by dividing the average power spectrum in (c2) (black squares) by the average power spectrum in (a2) (black squares). (c) Single-cell steady-state output $v_\infty(\varphi_0, x)$ (c1) and its power spectrum (c2). The analytical power spectrum in panel (c2) (black line) is derived in Section B.2 (Equations (A61), (A62), and (A68)). The power of the single-cell feedforward input is amplified by a factor $A_{\mathrm{cell}} \approx 7.9$ at the tuning harmonic $Lf = 5$ (Equation (A71)) and by a factor $A_{noise} \approx 1.2$ at all other frequencies (Equation (A67)). See Table A1 for parameter values

To quantify the improvement in spatial tuning, we compute the 1D grid-amplification index $\mathcal{A}$ as the ratio between the output and input 1D grid-tuning indexes. In Appendix B, we derive (Equations (A75) and (A76))

$$\mathcal{A} = \frac{A_{\text{cell}}}{A_{\text{noise}}} = \frac{B^2\frac{L}{4}(A_{\text{pop}}/A_{\text{noise}}) + (1-B)^2 S^{\xi}_{\text{cell}}(Lf)}{B^2\frac{L}{4} + (1-B)^2 S^{\xi}_{\text{cell}}(Lf)} \tag{A7}$$

where $S^{\xi}_{\text{cell}}(Lf)$ is the single-cell power of the input noise ξ at the tuning harmonic Lf. For $B = 0$, we obtain $\mathcal{A} = 1$, meaning that without a feedforward grid signal single-cell amplification is not possible (Equation (A7) and Figure A4a2). Conversely, for any $B > 0$, we obtain $\mathcal{A} > 1$, and the stronger the grid signal the larger the amplification. Finally, for $B \to 1$, the amplification index $\mathcal{A}$ approaches the asymptote $A_{\text{pop}}/A_{\text{noise}}$, where the factor A_{pop} is directly related to the maximal connection strength $M_{\max}$ (Equation (A6)), and the factor A_{noise} depends on the noise correlations across neurons (see next section).

We now compare these results (Figures A4a1,a2) with the ones obtained in the 2D model (Figure 4b,c). We observe that by increasing the input-tuning strength B, the grid-tuning index grows without bounds in the 1D model (Figure A4a1), but saturates in the 2D model (Figure 4b). As a result, the grid-amplification index is monotonic in 1D (Figure A4a2), but non-monotonic in 2D (Figure 4b). This is because in 2D (but not in 1D) a nonlinear activation function constrains the neural activity to non-negative values. In fact, by simulating the network activity of the 1D model with a threshold-linear activation function $F(x) := [x]_+$ (Equation (A1)), we recover the non-monotonic behavior of the grid-amplification index observed in 2D (compare Figure A4b1,b2 with Figure 4b,c).

A.2.2 | Effects of input correlations on grid-pattern amplification

In Section 2.4 of the main text (2D model), we showed that grid-pattern amplification crucially depends on the input-noise correlations across neurons. Here, this effect is reproduced in the 1D model and explained analytically. Figure A5a1 shows the 1D grid-tuning index as a function of the noise-correlation length σ_φ across neurons (Equation (A5)). Noise correlations across neurons do not affect the single-cell tuning at the feedforward input (Figure A5a1, magenta

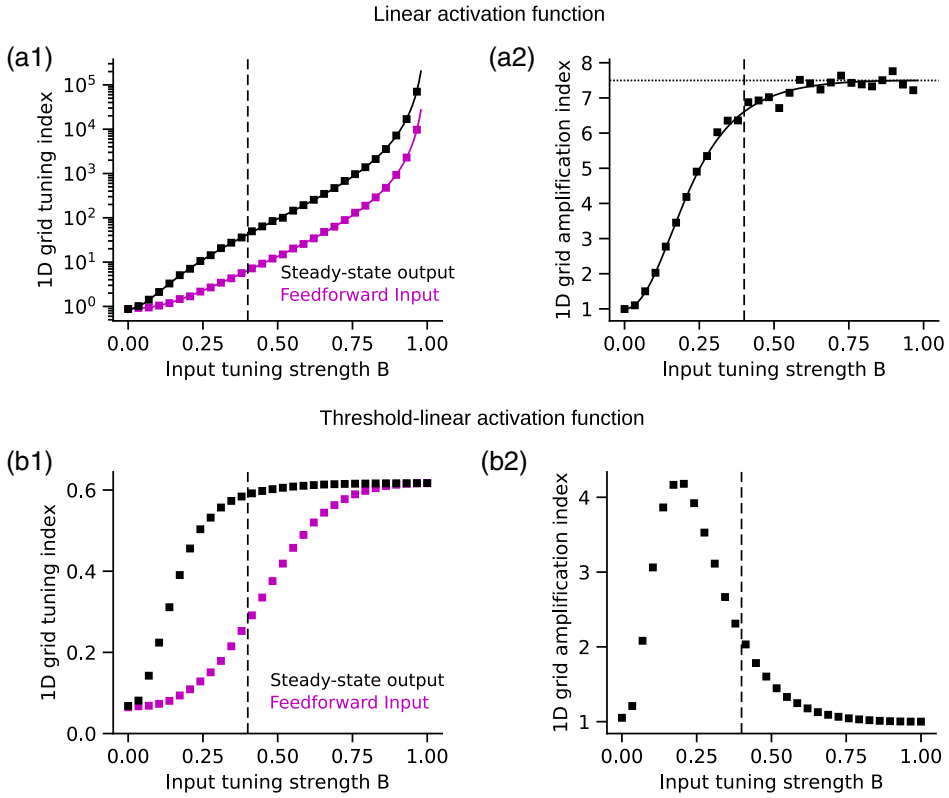

FIGURE A4 Effects of input tuning on grid-pattern amplification. (a) 1D grid-tuning index (a1) and 1D grid-amplification index (a2) as a function of the input-tuning strength B using a linear activation function $F(x) := x$ (Equation (A1)). In panel (a1), the 1D grid-tuning index is shown at the feedforward input (magenta) and steady-state output (black). Solid lines: analytical solutions (Equations (A38) and (A61)). Squares: numerical estimations computed by averaging 80 realizations of the input noise. The dashed vertical lines indicate the default input-tuning strength $B = 0.4$ used in Figures A2 and A3. In panel (a2), the 1D grid-amplification index $\mathcal{A}$ is defined as the ratio between output and input 1D grid-tuning indexes. Solid line: analytical solution (Equation (A7)). Squares: numerical estimation. The dotted horizontal line indicates the value of $A_{\text{pop}}/A_{\text{noise}} \approx 7.5$. (b) Same as in (a), but constraining the neural activity to be non-negative, that is, using a threshold-linear activation function $F(x) := [x]_+$ and increasing the maximal connection strength to $M_{\max} = 6$ (Equations (A1) and (A2)). See also Figure 4b,c for similar plots in the 2D model [Color figure can be viewed at wileyonlinelibrary.com]

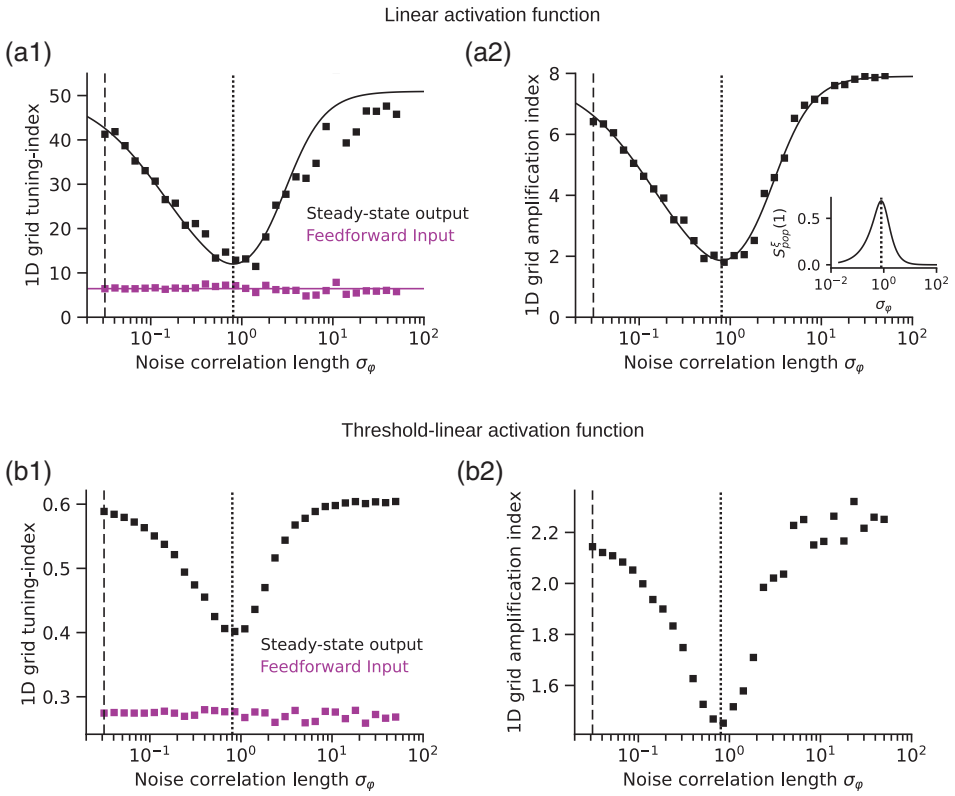

FIGURE A5 Effects of noise correlations across neurons on grid-pattern amplification. (a) 1D grid-tuning index (a1) and 1D grid-amplification index (a2) as a function of the noise-correlation length σ_φ using a linear activation function $F(x) := x$ (Equation (A1)). In panel (a1), the 1D grid-tuning index is shown at the feedforward input (magenta) and steady-state output (black). Solid lines: analytical solutions (Equations (A38) and (A61)). Squares: numerical estimations computed by averaging 80 realizations of the input noise. The dashed vertical lines indicate the default correlation length $\sigma_\varphi = 2\pi/N \approx 0.003$ (Figures A2 and A3), which corresponds to effectively uncorrelated noise. The dotted vertical line indicates the value of $\sigma_\varphi \approx 0.8$ at which the first harmonic of the population input noise $S^{\xi}_{\text{pop}}(1)$ is maximal. In panel (a2), the 1D grid-amplification index is defined as the ratio between output and input 1D grid-tuning indexes. Solid line: analytical solution (Equations (A7) and (A8)). Squares: numerical estimation. Inset: first harmonic of the population input noise $S^{\xi}_{\text{pop}}(1)$ as a function of the noise correlation length σ_φ. (b) Same as in (a), but using a threshold-linear activation function $F(x) = [x]_+$ and increasing the recurrent-connection strength to $M_{\max} = 6$ (Equations (A1) and (A2)). See also Figure 6b,c for similar plots in the 2D model [Color figure can be viewed at wileyonlinelibrary.com]

line), but control the single-cell tuning at the steady-state output (Figure A5a1, black line); see also Figure 6b for similar results in 2D. As a consequence, the 1D amplification index $\mathcal{A}$ is a non-monotonic function of σ_φ (Figure A5a2) and has a minimum at $\sigma_\varphi \approx 0.8$, where the first harmonic of the population input noise $S^{\xi}_{\text{pop}}(1)$ is maximal (inset of Figure A5a2, see also Figure 6c for similar results in 2D).

The dependency of the amplification index $\mathcal{A}$ on the noise correlation length σ_φ can be also understood analytically. Equation (A7) shows that the 1D grid-amplification index $\mathcal{A}$ is inversely related to the factor A_{noise}. In Appendix B (Equation (A67)), we derive

$$A_{\text{noise}} = 1 + \frac{A_{\text{pop}} - 1}{\pi/2} S^{\xi}_{\text{pop}}(1) \tag{A8}$$

where $S^{\xi}_{\text{pop}}(1)$ is the power of the population-input noise at the first harmonic. For uncorrelated noise ($\sigma_\varphi \to 0$) or fully correlated noise ($\sigma_\varphi \gg 1$), the noise power at the first harmonic is minimal ($S^{\xi}_{\text{pop}}(1) \ll 1$, inset of Figure A5a2) and A_{noise} approaches 1. In this scenario, the amplification index $\mathcal{A}$ is maximal and approaches A_{cell} (Equation (A7)). By contrast, for $\sigma_\varphi \approx 0.8$, the first harmonic of the input noise $S^{\xi}_{\text{pop}}(1)$ and the factor A_{noise} are maximal, and the amplification index $\mathcal{A}$ is minimal. Finally, we simulate the 1D model with a threshold-linear activation function to mimic the nonlinear activation used in 2D. This leads to results (Figure A5b1,b2) that are qualitatively similar to the ones obtained in the linear 1D model (Figure A5a1,a2) and the nonlinear 2D model (Figure 6c).

Finally, we study how single-cell amplification depends on the noise correlation length σ_x in space (see also Equation (A5)). Equation (A7) shows that the amplification index $\mathcal{A}$ is a function of $S^{\xi}_{\text{cell}}(Lf)$, which is the single-cell power of the input noise ξ at the tuning harmonic Lf. Because $S^{\xi}_{\text{cell}}(Lf)$ depends on σ_x (see also Equation (A42) in Appendix B), the index $\mathcal{A}$ also depends on σ_x. Note, however, that this dependency is weighted by the input-tuning strength $0 \le B \le 1$ (Equation (A7)). For $B \to 1$, the feedforward input approaches a perfect grid, the noise power approaches zero, and $\mathcal{A}$ is effectively independent of σ_x (Figure A6, right panel with $B = 0.8$). As B decreases, however, the noise power increases and $\mathcal{A}$ becomes weakly modulated by σ_x, see, for example, Figure A6 with $B = 0.4$ which was used in Figures A2, A3, and A5. For small values of B, the amplification index $\mathcal{A}$ is modulated by the noise-correlation length σ_x in space

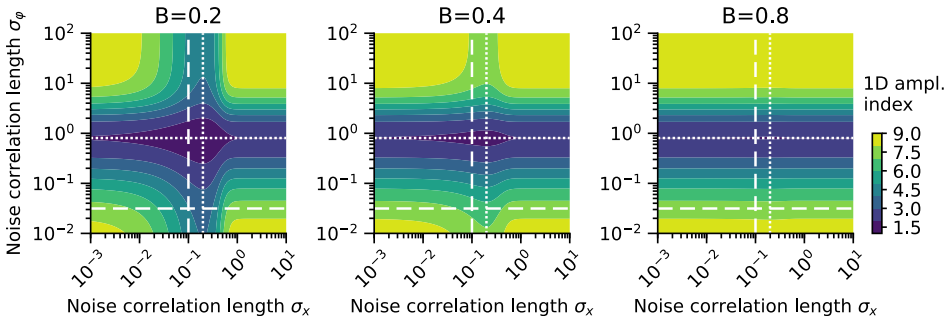

FIGURE A6 Effects of noise correlations in space and across neurons on grid-pattern amplification. The 1D grid-amplification index $\mathcal{A}$ (Equation (A7)) is plotted as function of the noise-correlation length in space (σ_x) and across neurons (σ_φ) for three values of the 1D input-tuning strength B (values at the top). The dashed lines denote default parameter values. The dotted horizontal lines denote the value of $\sigma_\varphi \approx 0.8$ for which the first harmonic of the population-input noise $S^{\xi}_{\text{pop}}(1)$ is maximal. The dotted vertical lines denote the value of $\sigma_x \approx 0.2$ for which the tuning harmonic Lf of the single-cell input-noise $S^{\xi}_{\text{cell}}(Lf)$ is maximal. Ampl., Amplification [Color figure can be viewed at wileyonlinelibrary.com]

almost as much as it is modulated by the noise-correlation length σ_φ across neurons (Figure A6, left panel with B = 0.2). Note, however, that for B = 0 the amplification index $\mathcal{A}$ = 1 is independent of both σ_x and σ_φ (Equation (A7)).

Finally, we find that for any B > 0 the amplification is minimal at the value of σ_x where the noise power $S^{\xi}_{\text{cell}}(Lf)$ is maximal (Figure A6, dotted vertical lines). In fact, in this case, the single-cell grid signal $g(\varphi_0, x)$ and the single-cell input noise $\xi(\varphi_0, x)$ maximally overlap in frequency domain, which is the worst-case scenario for amplification (see also Equations (A39) and (A42) in Appendix B).

APPENDIX B: Derivations for the one-dimensional grid-amplification model

Here, we provide the analytical derivations for the reduced 1D grid-amplification model in Appendix A. There we model the activity of a recurrent neural network that receives weakly grid-tuned feedforward inputs for a virtual rat running on a linear track. We recall that all input grids have the same spatial frequency f but different spatial phases φ. Assuming a linear activation function, the output activity v of a neuron with input phase φ is (Equation (A1) with $F(x) := x$)

$$\tau \frac{\mathrm{d}}{\mathrm{d}t} v(\varphi, x) := -v(\varphi, x) + h(\varphi, x) + \int_{-\pi}^{\pi} \mathrm{d}\varphi' M(\varphi - \varphi')\, v(\varphi', x) \tag{A9}$$

where x denotes a position on the track, h is the total feedforward input, the function M sets the recurrent connection strength, and τ > 0 controls the integration time constant of the network.

B.1 | Amplification at the population level

First, we study the network activity at the population level (see also Section A.1). To this end, we apply the complex Fourier series transformation

$$\tilde{f}_k := \int_{-\pi}^{\pi} \mathrm{d}\varphi f(\varphi) \exp(-jk\varphi) \quad \Leftrightarrow \quad f(\varphi) = \frac{1}{2\pi} \sum_{k=-\infty}^{\infty} \tilde{f}_k \exp(jk\varphi) \tag{A10}$$

at both sides of Equation (A9):

$$\tau \frac{\mathrm{d}}{\mathrm{d}t} \tilde{v}_k(x) = -\left(1 - \tilde{M}_k\right) \tilde{v}_k(x) + \tilde{h}_k(x) \tag{A11}$$

where $\tilde{v}_k \in \mathbb{C}$, $k \in \mathbb{Z}$, and $j = \sqrt{-1}$ is the imaginary unit. We note that the Fourier coefficients $\tilde{M}_k$ are the eigenvalues of the dynamical system in Equation (A9), and the corresponding eigenfunctions are the elements of the Fourier basis $e_k(\varphi) = \exp(jk\varphi)$.

Equation (A11) shows that for $\tilde{M}_k < 1 \forall k$, the output activity v converges to a stable fixed point v_∞ with Fourier coefficients

$$\tilde{v}^{\infty}_k(x) = \frac{1}{1 - \tilde{M}_k} \tilde{h}_k(x) = \tilde{F}^{\text{pop}}_k \tilde{h}_k(x) \tag{A12}$$

where the coefficients

$$\tilde{F}^{\text{pop}}_k := \frac{1}{1 - \tilde{M}_k} \tag{A13}$$

define the equivalent *population feedforward filter* of the network. Using the definition of the connectivity function $M(\varphi) := \frac{M_{\max}}{\pi} \cos(\varphi)$ in Equation (A2), we derive

$$\tilde{M}_k = \begin{cases} M_{\max} & \text{for } |k| = 1 \\ 0 & \text{otherwise} \end{cases} \quad \text{and} \quad \tilde{F}^{\text{pop}}_k = \begin{cases} \frac{1}{1\text{-}M_{\max}} & \text{for } |k| = 1 \\ 1 & \text{otherwise} \end{cases} \tag{A14}$$

where $M_{\max}$ > 0 is the maximal connection strength in the network. From Equation (A14), we compute the power spectrum

$$\left|\tilde{F}^{\text{pop}}_k\right|^2 = \begin{cases} A_{\text{pop}} & \text{for } |k| = 1 \\ 1 & \text{otherwise} \end{cases} \quad \text{with} \quad A_{\text{pop}} := \frac{1}{(1 - M_{\max})^2} \tag{A15}$$

of the equivalent population feedforward filter

$$F^{\text{pop}}(\varphi) \overset{(A10)}{=} \frac{1}{2\pi}\sum_{k=-\infty}^{\infty}\tilde{F}_k^{\text{pop}}\exp(jk\varphi) \overset{(A15)}{=} \frac{\sqrt{A_{\text{pop}}}-1}{\pi}\cos(\varphi)+\delta(\varphi) \quad \text{(A16)}$$

where δ is Dirac's delta.

B.1.1 | Population-level power spectra

We now compute the population-level power spectra of the feedforward input h and of the steady-state output v_∞ (see also Section A.1 and Figure A2). We recall that the feedforward input h is a weighted sum of a grid signal g and a noise term ξ (Equation (A3))

$$h(\varphi,x) := Bg(\varphi,x)+(1-B)\xi(\varphi,x) \quad \text{with} \quad g(\varphi,x) := \cos(2\pi fx+\varphi) \quad \text{(A17)}$$

where the parameter $0 \le B \le 1$ controls the input-tuning strength. We also recall that the noise ξ has autocorrelation (Equation (A5))

$$C_\xi(\tau_\varphi,\tau_x) := \langle \xi(\varphi,x)\xi(\varphi+\tau_\varphi,x+\tau_x)\rangle_{\varphi,x} \quad \text{(A18)}$$

$$= \frac{1}{2}\mathcal{M}(\tau_\varphi;\sigma_\varphi)\mathcal{M}(2\pi\tau_x/L;\sigma_x) \quad \text{(A19)}$$

where angular brackets denote statistical expectation and

$$\mathcal{M}(\tau,\sigma) := \exp\left(\frac{\cos(\tau)-1}{\sigma^2}\right) \quad \text{(A20)}$$

is a von Mises function with spread $\sigma > 0$. In Equation (A19), the parameters $\sigma_\varphi > 0$ and $\sigma_x > 0$ control the noise-correlation length across neurons and across space, respectively.

Population-level input power spectrum

We define the population-level input power spectrum

$$S^h_{\text{pop}}(k) := \int_{-\pi}^{\pi} d\tau C^h_{\text{pop}}(\tau)\exp(-jk\tau) \quad \text{with} \quad k\in\mathbb{Z} \quad \text{(A21)}$$

where

$$C^h_{\text{pop}}(\tau) := \langle h(\varphi,x)\, h(\varphi+\tau,x)\rangle_\varphi \quad \text{(A22)}$$

$$\overset{(A17)}{=} B^2\underbrace{\langle g(\varphi,x)g(\varphi+\tau,x)\rangle_\varphi}_{=:C^g_{\text{pop}}(\tau)} + (1-B)^2\underbrace{\langle \xi(\varphi,x)\xi(\varphi+\tau,x)\rangle_\varphi}_{=:C^\xi_{\text{pop}}(\tau)} \quad \forall x \quad \text{(A23)}$$

is the population-level autocorrelation of the feedforward input h (Equation (A17)). Because signal and noise are independent and zero-mean, the cross terms of the product in Equation (A22) vanish. In Equation (A23), the functions $C^g_{\text{pop}}(\tau)$ and $C^\xi_{\text{pop}}(\tau)$ are the population-level autocorrelations of the input signal g and the input noise ξ, which are independent of the virtual-rat position x on the track:

$$C^g_{\text{pop}}(\tau) = \frac{1}{2\pi}\int_{-\pi}^{\pi} d\varphi g(\varphi,x)g(\varphi+\tau,x) \overset{(A17)}{=} \frac{\cos(\tau)}{2} \quad \text{(A24)}$$

and

$$C^\xi_{\text{pop}}(\tau) \overset{(A18)}{=} C_\xi(\tau,0) \overset{(A19)}{=} \frac{1}{2}\mathcal{M}(\tau;\sigma_\varphi). \quad \text{(A25)}$$

From Equations (A21) and (A23), we find that the population-level power spectrum S^h_{pop} of the feedforward input h is a weighted sum of the population-level power spectra S^g_{pop} and S^ξ_{pop}. That is,

$$S^h_{\text{pop}}(k) = B^2S^g_{\text{pop}}(k) + (1-B)^2S^\xi_{\text{pop}}(k) \quad \text{(A26)}$$

where

$$S^g_{\text{pop}}(k) := \int_{-\pi}^{\pi} d\tau\, C^g_{\text{pop}}(\tau)\exp(-jk\tau) \overset{(A24)}{=} \begin{cases}\pi/2 & \text{for } |k| = 1\\ 0 & \text{otherwise}\end{cases} \quad \text{(A27)}$$

and

$$S^\xi_{\text{pop}}(k) := \int_{-\pi}^{\pi} d\tau\, C^\xi_{\text{pop}}(\tau)\exp(-jk\tau) \quad \text{(A28)}$$

$$\overset{(A25)}{=} \frac{1}{2}\tilde{\mathcal{M}}(k;\sigma_\varphi). \quad \text{(A29)}$$

In Equation (A29), $\tilde{\mathcal{M}}(k,\sigma_\varphi)$ is the k^{th} harmonic of the complex Fourier series (Equation (A10)) of the function $\mathcal{M}(\tau;\sigma_\varphi)$ (Equation (A20)). That is,

$$\tilde{\mathcal{M}}(k;\sigma_\varphi) := \int_{-\pi}^{\pi} d\tau\mathcal{M}(\tau;\sigma_\varphi)\exp(-jk\tau) = \pi\exp\left(-\frac{1}{\sigma_\varphi^2}\right)I_k\left(\frac{1}{\sigma_\varphi^2}\right) \quad \text{(A30)}$$

where

$$I_k(z) := \frac{1}{\pi}\int_0^{\pi} d\theta\exp[z\cos(\theta)]\cos(k\theta) \quad \text{(A31)}$$

is the kth-order modified Bessel funpaction of the first kind.

Population-level output power spectrum

In Equations (A12)–(A15), we showed that at the steady-state output the input power S^h_{pop} is amplified by a factor A_{pop} at the first harmonic. Therefore, the population-level power spectrum at the steady-state output is

$$S^{v_\infty}_{\text{pop}}(k) = \begin{cases}A_{\text{pop}}S^h_{\text{pop}}(k) & \text{for } |k| = 1\\ S^h_{\text{pop}}(k) & \text{otherwise.}\end{cases} \quad \text{(A32)}$$

B.2 | Amplification at the single-cell level

To quantify grid-pattern amplification at the single-cell level, we now compute the single-cell power spectra at the feedforward input h and steady-state output v_∞ (see also Section A.2 and Figure A3).

B.2.1 | Single-cell power spectra

Single-cell input power spectrum

We define the single-cell input power spectrum

$$S^h_{\text{cell}}(k) := \int_{-L/2}^{L/2} \mathrm{d}\tau\, C^h_{\text{cell}}(\tau) \exp\left(-\frac{j2\pi k\tau}{L}\right) \tag{A33}$$

where L is the length of the track and

$$C^h_{\text{cell}}(\tau) := \langle h(\varphi,x)\, h(\varphi,x+\tau)\rangle_x \tag{A34}$$

$$\overset{(A17)}{=} B^2 \underbrace{\langle g(\varphi,x)g(\varphi,x+\tau)\rangle_x}_{=:C^g_{\text{cell}}(\tau)} + (1-B)^2 \underbrace{\langle \xi(\varphi,x)\xi(\varphi,x+\tau)\rangle_x}_{=:C^\xi_{\text{cell}}(\tau)} \quad \forall\varphi \tag{A35}$$

is the single-cell autocorrelation of the feedforward input h. In Equation (A35), the functions $C^g_{\text{cell}}(\tau)$ and $C^\xi_{\text{cell}}(\tau)$ are the single-cell autocorrelations of the input signal g and the input noise ξ, which are independent of the preferred phase φ:

$$C^g_{\text{cell}}(\tau) = \frac{1}{L}\int_{-L/2}^{L/2} \mathrm{d}x\, g(\varphi,x)g(\varphi,x+\tau) \overset{(A17)}{=} \frac{\cos(2\pi f\tau)}{2} \tag{A36}$$

and

$$C^\xi_{\text{cell}}(\tau) \overset{(A18)}{=} C_\xi(0,\tau) \overset{(A19)}{=} \frac{1}{2}\mathcal{M}(2\pi\tau/L;\sigma_x). \tag{A37}$$

From Equations (A33) and (A35), we obtain

$$S^h_{\text{cell}}(k) = B^2 S^g_{\text{cell}}(k) + (1-B)^2 S^\xi_{\text{cell}}(k) \tag{A38}$$

where

$$S^g_{\text{cell}}(k) := \int_{-L/2}^{L/2} \mathrm{d}\tau\, C^g_{\text{cell}}(\tau) \exp\left(-\frac{j2\pi k\tau}{L}\right) \overset{(A36)}{=} \begin{cases} L/4 & \text{for } |k| = Lf \\ 0 & \text{otherwise} \end{cases} \tag{A39}$$

and

$$S^\xi_{\text{cell}}(k) := \int_{-L/2}^{L/2} \mathrm{d}\tau\, C^\xi_{\text{cell}}(\tau) \exp\left(-\frac{j2\pi k\tau}{L}\right) \tag{A40}$$

$$\overset{(A37)}{=} \frac{1}{2}\int_{-L/2}^{L/2} \mathrm{d}\tau\, \mathcal{M}\left(\frac{2\pi\tau}{L};\sigma_x\right) \exp\left(-\frac{j2\pi k\tau}{L}\right) \tag{A41}$$

$$= \frac{L}{4\pi}\tilde{\mathcal{M}}(k;\sigma_x). \tag{A42}$$

Steady-state output

To compute the single-cell output power spectrum, we first compute the steady-state output v_∞. In Section B.1 (Equation (A12)), we derived the Fourier coefficients

$$\tilde{v}^\infty_k(x) = \tilde{F}^{\text{pop}}_k\, \tilde{h}_k(x) \tag{A43}$$

where

$$\tilde{F}^{\text{pop}}_k \overset{(A15)}{=} \begin{cases} \sqrt{A_{\text{pop}}} & \text{for } |k| = 1 \\ 1 & \text{otherwise} \end{cases} \tag{A44}$$

are the Fourier coefficients of the equivalent population feedforward filter F^{pop} (Equations (A14) and (A15)). By back-transforming Equation (A43) to phase domain, we obtain (Equation (A10))

$$v_\infty(\varphi,x) = \int_{-\pi}^{\pi} \mathrm{d}\tau\, h(\tau,x)F^{\text{pop}}(\varphi-\tau) \tag{A45}$$

$$\overset{(A17)}{=} B\underbrace{\int_{-\pi}^{\pi} \mathrm{d}\tau g(\tau,x)F^{\text{pop}}(\varphi-\tau)}_{=:g^{\text{out}}(\varphi,x)} + (1-B)\underbrace{\int_{-\pi}^{\pi} \mathrm{d}\tau\, \xi(\tau,x)F^{\text{pop}}(\varphi-\tau)}_{=:\xi^{\text{out}}(\varphi,x)} \tag{A46}$$

where g^{out} is the output signal and ξ^{out} is the output noise. The output signal

$$g^{\text{out}}(\varphi,x) = \frac{1}{2\pi}\sum_{k=-\infty}^{\infty} \tilde{g}_k(x)\tilde{F}^{\text{pop}}_k \exp(j\varphi k) \overset{(A44)}{=} \sqrt{A_{\text{pop}}}\, g(\varphi,x) \tag{A47}$$

has single-cell autocorrelation

$$C^{g^{\text{out}}}_{\text{cell}}(\tau) = \frac{1}{L}\int_{-L/2}^{L/2} \mathrm{d}x g^{\text{out}}(\varphi,x)g^{\text{out}}(\varphi,x+\tau) \overset{(A47)}{=} A_{\text{pop}}\, C^g_{\text{cell}}(\tau). \tag{A48}$$

Output noise

We now compute the autocorrelation of the output noise ξ^{out}:

$$C_{\xi^{\text{out}}}(\tau_\varphi,\tau_x) := \left\langle \xi^{\text{out}}(\varphi,x)\xi^{\text{out}}\left(\varphi+\tau_\varphi,x+\tau_x\right)\right\rangle_{\varphi,x} \tag{A49}$$

$$= \frac{1}{2\pi}\int_{-\pi}^{\pi} \mathrm{d}\varphi \frac{1}{L}\int_{-L/2}^{L/2} \mathrm{d}x\, \xi^{\text{out}}(\varphi,x)\, \xi^{\text{out}}\left(\varphi+\tau_\varphi,x+\tau_x\right) \tag{A50}$$

$$= \int_{-\pi}^{\pi} \mathrm{d}\varphi\, C_\xi(\tau_\varphi-\varphi,\tau_x)\int_{-\pi}^{\pi} \mathrm{d}\varphi' F^{\text{pop}}(\varphi')F^{\text{pop}}(\varphi+\varphi') \tag{A51}$$

where in Equation (A51) we used the definition of the output noise ξ^{out} (Equation (A46)) and the definition of the input-noise autocorrelation C_ξ (Equation (A18)). Equation (A51) shows that $C_{\xi^{\text{out}}}$ is obtained by convolving the input-noise autocorrelation C_ξ with the autocorrelation of the population filter F^{pop}:

$$\int_{-\pi}^{\pi} d\varphi' F^{pop}(\varphi') F^{pop}(\varphi+\varphi') = \frac{1}{2\pi}\sum_{k=-\infty}^{\infty} \left|\tilde{F}_k^{pop}\right|^2 \exp(jk\varphi) \tag{A52}$$

$$\overset{(A12)}{=} \frac{A_{pop}-1}{\pi}\cos(\varphi) + \delta(\varphi). \tag{A53}$$

Therefore, from Equations (A51) and (A53), we obtain

$$C_{\xi^{out}}(\tau_\varphi,\tau_x) = C_\xi(\tau_\varphi,\tau_x) + \frac{A_{pop}-1}{\pi}\int_{-\pi}^{\pi} d\varphi\, C_\xi(\tau_\varphi-\varphi,\tau_x)\cos(\varphi). \tag{A54}$$

Plugging Equation (A19) into Equation (A54) yields

$$\int_{-\pi}^{\pi} d\varphi\, C_\xi(\tau_\varphi-\varphi,\tau_x)\cos(\varphi) = \frac{1}{2}\mathcal{M}\left(\frac{2\pi\tau_x}{L};\sigma_x\right)\int_{-\pi}^{\pi} d\varphi\, \mathcal{M}(\tau_\varphi-\varphi;\sigma_\varphi)\cos(\varphi) \tag{A55}$$

$$= \frac{1}{2}\mathcal{M}\left(\frac{2\pi\tau_x}{L};\sigma_x\right)\cos(\tau_\varphi)\tilde{\mathcal{M}}(1;\sigma_\varphi). \tag{A56}$$

Finally, using Equations (A19) and (A56) in Equation (A54) yields

$$C_{\xi^{out}}(\tau_\varphi,\tau_x) = \frac{1}{2}\mathcal{M}\left(\frac{2\pi\tau_x}{L};\sigma_x\right)\left[\mathcal{M}(\tau_\varphi;\sigma_\varphi) + \frac{A_{pop}-1}{\pi}\cos(\tau_\varphi)\tilde{\mathcal{M}}(1;\sigma_\varphi)\right]. \tag{A57}$$

Equation (A57) shows that the recurrent dynamics affects the noise correlations across neurons (τ_φ) but not across space (τ_x)

Single-cell output power spectrum

Here, we compute the single-cell output power spectrum

$$S_{cell}^{v^\infty}(k) := \int_{-L/2}^{L/2} d\tau\, C_{cell}^{v^\infty}(\tau)\exp\left(-\frac{j2\pi k\tau}{L}\right) \tag{A58}$$

where the single-cell autocorrelation of the steady-state output is

$$C_{cell}^{v^\infty}(\tau) := \langle v^\infty(\varphi,x)\, v^\infty(\varphi,x+\tau)\rangle_x \tag{A59}$$

$$\overset{(A46)}{=} B^2 \underbrace{\langle g^{out}(\varphi,x) g^{out}(\varphi,x+\tau)\rangle_x}_{=:C_{cell}^{g^{out}}(\tau)} + (1-B)^2 \underbrace{\langle \xi(\varphi,x)\xi(\varphi,x+\tau)\rangle_x}_{=:C_{cell}^{\xi^{out}}(\tau)} \quad \forall\varphi. \tag{A60}$$

Using Equation (A60) in Equation (A58) yields:

$$S_{cell}^{v^\infty}(k) = B^2 S_{cell}^{g^{out}}(k) + (1-B)^2 S_{cell}^{\xi^{out}}(k) \tag{A61}$$

where $S_{cell}^{g^{out}}$ is the single-cell power spectrum of the output signal and $S_{cell}^{\xi^{out}}$ is the single-cell power spectrum of the output noise. We derive

$$S_{cell}^{g^{out}}(k) := \int_{-L/2}^{L/2} d\tau\, C_{cell}^{g^{out}}(\tau)\exp\left(-\frac{j2\pi k\tau}{L}\right) \overset{(A48)}{=} A_{pop}\, S_{cell}^{g}(k). \tag{A62}$$

To compute the power spectrum $S_{cell}^{\xi^{out}}$, we first compute the single-cell autocorrelation

$$C_{cell}^{\xi^{out}}(\tau) := \langle \xi^{out}(\varphi,x)\, \xi^{out}(\varphi,x+\tau)\rangle_x \tag{A63}$$

$$\overset{(A49)}{=} C_{\xi^{out}}(0,\tau) \tag{A64}$$

$$\overset{(A57)}{=} \frac{1}{2}\mathcal{M}\left(\frac{2\pi\tau_x}{L};\sigma_x\right)\left[1+\frac{A_{pop}-1}{\pi}\tilde{\mathcal{M}}(1;\sigma_\varphi)\right] \tag{A65}$$

$$\overset{(A37)}{=} A_{noise} C_{cell}^{\xi}(\tau) \tag{A66}$$

where

$$A_{noise} := 1 + \frac{A_{pop}-1}{\pi}\tilde{\mathcal{M}}(1;\sigma_\varphi) \overset{(A29)}{=} 1 + \frac{A_{pop}-1}{\pi/2} S_{pop}^{\xi}(1). \tag{A67}$$

Therefore, the single-cell power spectrum of the output noise reads

$$S_{cell}^{\xi^{out}}(k) := \int_{-L/2}^{L/2} d\tau\, C_{cell}^{\xi^{out}}(\tau)\exp\left(-\frac{j2\pi k\tau}{L}\right) \overset{(A66)}{=} A_{noise} S_{cell}^{\xi}(k). \tag{A68}$$

Equations (A62) and (A68) show that the power of the input signal is amplified by a factor A_{pop} (Equation (A15)) whereas the power of the input noise is amplified by a factor A_{noise} (Equation (A67)). Therefore, at the single-cell level, the effects of the recurrent connections on the network activity are summarized by the power $\left|\tilde{F}_k^{cell}\right|^2$ of the equivalent *single-cell feedforward* filter F^{cell}. That is

$$\left|\tilde{F}_k^{cell}\right|^2 := \frac{S_{cell}^{v^\infty}(k)}{S_{cell}^{h}(k)} = \frac{B^2 A_{pop} S_{cell}^{g}(k) + (1-B)^2 A_{noise} S_{cell}^{\xi}(k)}{B^2 S_{cell}^{g}(k) + (1-B)^2 S_{cell}^{\xi}(k)} \tag{A69}$$

where in Equation (A69) we used Equations (A38), (A61), (A62), and (A68). Because the grid signal g has power only at the tuning frequency $k = Lf$ (Equation (A39)), we can rewrite Equation (A69) as follows:

$$\left|\tilde{F}_k^{cell}\right|^2 := \frac{S_{cell}^{v^\infty}(k)}{S_{cell}^{h}(k)} = \begin{cases} A_{cell} & \text{for } k = Lf \\ A_{noise} & \text{otherwise} \end{cases} \tag{A70}$$

where

$$A_{cell} := \frac{B^2 A_{pop} S_{cell}^{g}(Lf) + (1-B)^2 A_{noise} S_{cell}^{\xi}(Lf)}{B^2 S_{cell}^{g}(Lf) + (1-B)^2 S_{cell}^{\xi}(Lf)}. \tag{A71}$$

Equation (A70) shows that, at the single-cell level, the input power is amplified by a factor A_{cell} at the tuning harmonic $k = Lf$, and by a factor A_{noise} at all other frequencies. From Equation (A70), we derive

$$F^{cell}(x) = \frac{1}{L}\sum_{k=-\infty}^{\infty} \tilde{F}_k^{cell}\exp\left(\frac{j2\pi kx}{L}\right) \tag{A72}$$

$$= \sqrt{A_{\text{noise}}}\,\delta(x) + \frac{2}{L}\left(\sqrt{A_{\text{cell}}} - \sqrt{A_{\text{noise}}}\right)\cos(2\pi f x). \tag{A73}$$

B.2.2 | One-dimensional amplification index

To quantify grid tuning at the single-cell level, in Appendix A we define the 1D grid-tuning index as single-cell activity power at the tuning harmonic (Lf) normalized by the single-cell activity power at the zeroth harmonic. We then measure the improvement in grid tuning by computing the 1D amplification index

$$\mathcal{A} := \frac{S^{v_\infty}_{\text{cell}}(Lf)/S^{v_\infty}_{\text{cell}}(0)}{S^{h}_{\text{cell}}(Lf)/S^{h}_{\text{cell}}(0)} \tag{A74}$$

where the nominator is the 1D grid-tuning index at the steady-state output v_∞ and the denominator is the 1D grid-tuning index at the feedforward input h. From Equation (A74), we derive

$$\mathcal{A} = \frac{S^{v_\infty}_{\text{cell}}(Lf)/S^{h}_{\text{cell}}(Lf)}{S^{v_\infty}_{\text{cell}}(0)/S^{h}_{\text{cell}}(0)} \overset{(A70)}{=} \frac{A_{\text{cell}}}{A_{\text{noise}}}. \tag{A75}$$

Finally, by using Equations (A39) and (A71) in Equation (A75), we obtain:

$$\mathcal{A} = \frac{A_{\text{cell}}}{A_{\text{noise}}} = \frac{B^2\frac{L}{4}(A_{\text{pop}}/A_{\text{noise}}) + (1-B)^2 S^{\xi}_{\text{cell}}(Lf)}{B^2\frac{L}{4} + (1-B)^2 S^{\xi}_{\text{cell}}(Lf)}. \tag{A76}$$